DIAGNOSIS AND ISOLATION OF AIR GAP ECCENTRICITIES IN CLOSED-LOOP CONTROLLED DOUBLY-FED INDUCTION GENERATORS

A Thesis

by

VIVEK MEENAKSHI SUNDARAM

Submitted to the Office of Graduate Studies of
Texas A&M University
in partial fulfillment of the requirements for the degree of

MASTER OF SCIENCE

May 2011

Major Subject: Electrical Engineering

Diagnosis and Isolation of Air Gap Eccentricities in Closed-Loop Controlled

Doubly-Fed Induction Generators

DIAGNOSIS AND ISOLATION OF AIR GAP ECCENTRICITIES IN CLOSED-LOOP CONTROLLED DOUBLY-FED INDUCTION GENERATORS

A Thesis

by

VIVEK MEENAKSHI SUNDARAM

Submitted to the Office of Graduate Studies of
Texas A&M University
in partial fulfillment of the requirements for the degree of

MASTER OF SCIENCE

Approved by:

Chair of Committee,	Hamid Toliyat
Committee Members,	Mehrdad Ehsani
	Shankar Bhattacharyya
	Won-Jong Kim
Head of Department,	Costas N. Georghiades

May 2011

Major Subject: Electrical Engineering

ABSTRACT

Diagnosis and Isolation of Air Gap Eccentricities in Closed-loop Controlled Doubly-Fed Induction Generators.

(May 2011)

Vivek Meenakshi Sundaram, B.Tech., National Institute of Technology, Trichy

Chair of Advisory Committee: Dr. Hamid Toliyat

With the widespread use of doubly-fed induction generators (DFIG) in wind energy conversion systems, condition monitoring is being given importance. Non-intrusive techniques like motor current signature analysis (MCSA), which involves looking for specific frequency components in the current spectrum, are preferred over analysis of magnetic field, temperature, vibrations or acoustic noise which require additional sensors. The major difficulty in MCSA is isolation of the fault, as multiple faults produce similar signatures. Moreover, closed-loop control makes diagnostics more complicated due to inherent compensation by the controller.

This thesis presents a method to diagnose static and dynamic air gap eccentricities in doubly-fed induction generators operated for closed-loop stator power control by using a modified control technique to enable detection and isolation of this fault from electrical unbalances in the stator and rotor and load torque oscillations that produce similar effects. The effectiveness of the proposed control is verified using simulations and preliminary experiments performed on a healthy machine.

To my parents

ACKNOWLEDGEMENTS

First, I thank my advisor Dr. Hamid Toliyat for all the motivation, encouragement and support he has given me throughout the course of this research. He has been an endless source of inspiration for me and I feel honored to be able to work with him. I am looking forward to completing my graduate studies under his supervision.

I thank my committee members Dr. Mehrdad Ehsani, Dr. Shankar Bhattacharyya and Dr.Won-Jong Kim for their valuable time. I have learned a lot from their courses.

I thank my colleagues at the Advanced Electric Machines and Power Electronics Lab, Robert Vartanian, Nicholas Frank, Yateendra Deshpande, Mahshid Amirabadi, Siavash Pakdelian, Seung Deog Choi, Babak Farhangi, Anil Chakali and Behrooz Nikbakhtian. A special thanks to Yateendra Deshpande for his valuable help during the course of the project. I also thank all my friends who made life in College Station a little easier.

Finally, I thank my parents and brother for all their emotional and monetary support and guidance.

TABLE OF CONTENTS

Page

Page

LIST OF FIGURES

Page

Page

Page

LIST OF TABLES

Page

1. INTRODUCTION AND LITERATURE REVIEW

Wind energy is rapidly becoming the most promising renewable energy source. According to the US Department of Energy, in 2009 a record 10,010 MW of wind installations were made, representing 39% of the US electrical generation capacity additions for the year. The total wind installations by the end of 2009 were more than 35,000 MW which reduced the amount of CO_2 emissions by 62 million tons annually [1]. Wind energy installations are growing in number at the rate of 20% to 30% every year in the US and Europe [2]. The increase in wind capacity has been accompanied by improved reliability, lower capital costs and better efficiency. With enormous wind potential available both on-shore and off-shore, efforts are being made to enable smooth grid interconnection that will provide utilities with a cleaner alternative which is not sensitive to fuel price hikes.

1.1 Classification of wind energy conversion systems

Wind turbine systems are comprised of the generator, gear-box and the power electronic converter. The above three components put together account for 25% of the cost of the turbine [1]. There are different configurations for the electrical system of the wind turbines depending on the type of electric machine that is used for generation. Both synchronous and induction machines have been extensively used in wind turbine applications, each with their own advantages and disadvantages.

This thesis follows the style of *IEEE Transactions on Magnetics.*

The mechanical power captured from the wind is given by [3]

$$P = 0.5\rho\pi R^2 C_p v^3 \tag{1.1}$$

ρ = density of air

R = radius of the turbine blade

C_p = power coefficient

v = wind velocity

The wind turbine should be operated at maximum C_p at all wind speeds to ensure maximum efficiency. C_p is a function of pitch angle, β and tip speed ratio, λ, which is the ratio of the turbine speed and the wind speed. To maintain optimal λ, the turbine speed has to be increased with increase in wind speed.

Wind energy conversion systems can be classified into two categories:

- Fixed speed systems
- Variable speed systems

Fixed speed systems mostly use self-excited induction generators (SEIGs) shown in Fig. 1. These are essentially squirrel-cage induction machines with three-phase capacitor banks on the stator to provide the reactive power required for magnetization of the stator. A cage induction machines should operate above synchronous speed for generating operation. Hence the machine is always operated over a narrow range of negative slip which is imposed by the grid frequency. This is usually achieved by pitch and yaw control to maintain the shaft speed relatively constant with variations in wind speed. SEIGs operate at maximum efficiency only at their rated wind speeds, but these

systems are low cost and robust. Systems using SEIGs can be used for both stand-alone and grid connected operations of wind turbines.

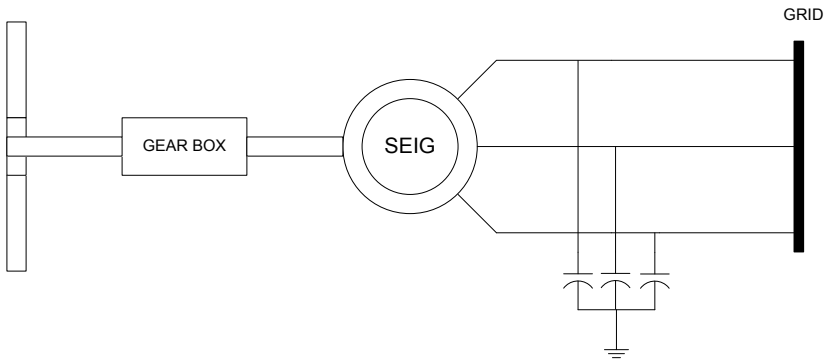

Fig. 1. Wind energy conversion system using cage rotor induction generator

SEIGs can also be used in variable speed systems by adding a frequency converter between the stator and grid. However the power rating of the converter should be the same as the power rating of the machine.

In variable speed systems the turbine speed is varied with wind speed to ensure constant, maximum C_p operation and hence maximum efficiency. This is achieved by means of a power electronic converter in doubly-fed induction generators (DFIGs) as shown in Fig. 2. Since the rotor handles only the slip power, which is a fraction of the power flowing through the stator, the size of the converter is much smaller when compared to the SEIG for a ±40% range of operating slip. This significantly improves efficiency due to lower switching and conduction losses. However DFIGs have additional problems due to the presence of brushes.

Salient-pole permanent magnet synchronous generators (PMSG) are also used for variable speed generation systems. Such a system is shown in Fig. 3**.** Here there is no need for any rotor excitation and the machine can be operated at low speeds without the need for a gear box.

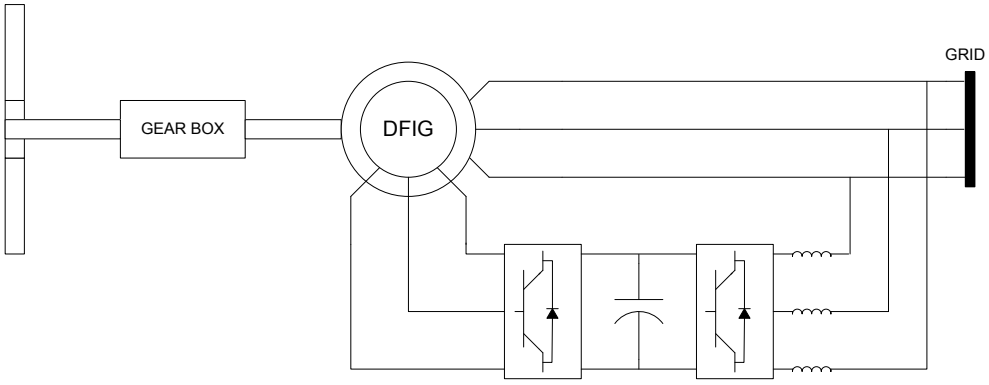

Fig. 2. DFIG based wind energy conversion system

However the rating of the frequency converter should be the same as the generator leading to greater switching and conduction losses in the power electronic system. The gear-box has however been identified as one of the major sources of failure of wind energy systems which is the reason PMSG conversion systems are growing in popularity. Systems using PMSG are also called direct drive systems due to the elimination of the gear-box [4].

Among the above mentioned topologies the DFIG is preferred at power levels of up to 1.5MW because they use smaller sized converters and are hence more efficient. This thesis deals with variable speed wind energy conversion systems using DFIGs for power generation.

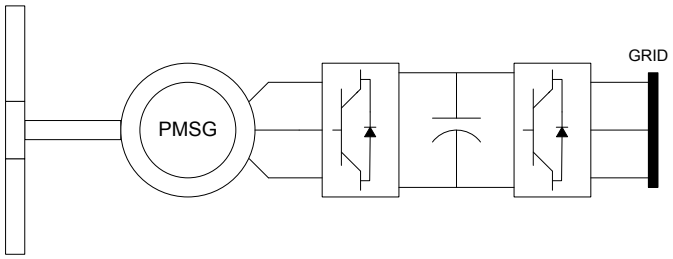

Fig. 3. Direct drive PMSG based wind energy conversion system

1.2 Fault diagnosis of electric machines- A literature review

The major faults that occur in induction machines are [5]

1. Stator electrical faults, which includes shorting or opening of windings (also called stator inter-turn faults)
2. Rotor electrical faults which includes broken bar, end ring cracking and winding shorts
3. Air gap eccentricity due to irregularities or bearing failure
4. Gear-box/bearing failure

Stator electric faults constitute 30-40% of motor faults. These faults are primarily caused by insulation failure resulting in shorting between the stator turns. Broken bar and end-ring faults are caused due to mechanical stresses acting on the rotor cage. These faults constitute 5-10% of induction motor failures [5].

Bearings used in electric machines are either ball or rolling element bearings with a ring structure. Bearing faults result primarily from fatigue failure which damage different parts of the bearing. Bearing faults may result in air gap eccentricities and vibrations in the machine. They are sub classified into inner bearing race defect, outer

bearing race defect and ball defect [5]. Of these 40-50% of motor faults are caused by bearing failure. Air gap eccentricities can be caused either by a misalignment between the centers of the rotor and the stator or by the presence of any irregularities in the rotor periphery or inner wall of the stator. Air gap eccentricities lead to a non-uniform air gap between the rotor and stator and hence an unbalanced radial magnetic pull on the rotor.

Air gap eccentricities are classified into two types:

1. Static air gap eccentricities are caused due to irregularities, displacement or oval nature of rotor. Here the centers of the stator and rotor coincide but the air gap is not uniform around the rotor periphery. So there are fixed points of minimum and maximum air gap width around the rotor.
2. Dynamic eccentricities are characterized by misalignment between the centers of the rotor and stator. The point of minimum air gap rotates around the center of the stator. Dynamic eccentricities can be caused by bending of the shaft, bearing failure or mechanical resonance.

Up to 10% eccentricity on the rotor is considered as permissible. Static and dynamic eccentricities can also exist together. While machines are manufactured with a small level of static eccentricity, the unbalanced magnetic pull that results from this causes a gradual bending in the rotor shaft leading to dynamic eccentricity [5]. This is sometimes referred to as mixed eccentricity in the literature.

Several methods have been used for detection and identification of these faults. Each method involves monitoring specific quantities which provide indices to detect and

identify the fault. These techniques can be typically categorized into invasive and non-invasive techniques.

Invasive techniques involve external installations on the machine for sensing purposes. Vibration sensing has been used for detection of bearing and eccentricity related faults [6]. Vibration measurements are usually made using accelerometers or displacement probes to monitor shaft movements. Electrical asymmetries in the stator and rotor can be detected by measuring the axial flux in the air gap using search coils wound around the shaft of the machine [7]. Symmetrical positioning of the search coils has been used to determine the position of the fault.

The most commonly used non- invasive technique is motor current signature analysis (MCSA). This involves monitoring specific frequency components in the current spectrum that are caused by the fault. The disadvantage of this technique is that most frequency components are not exclusive to a single type of fault. This makes it difficult to isolate the fault after diagnosis. Another drawback of MCSA is in condition monitoring of closed-loop controlled systems. In such systems the effect of the fault is compensated by the controller and the extent of compensation depends on the frequency response characteristic of the closed-loop system [8]. This has led to the development of modified diagnosis methods that are specific to the system. In [9], the authors have found that for induction machines operated using closed-loop current control, the d-axis stator current is fairly independent of controller gains and dependent on fault degree, thus serving as a good index for diagnosis. This is used for detecting electrical faults in the stator and rotor by monitoring the *2f* and *2sf* frequency components. The rotor

modulating signals are used to detect stator and rotor unbalances in a DFIG with a voltage source inverter connected to the rotor in [10]. This is based on the assumption that in closed-loop operation with stator flux oriented control, the control system will try to compensate the effect of stator unbalance and this can be detected in the modulating signals generated by the rotor side controller. The effect of load torque oscillations on the current spectrum has been investigated in [11] where it has been shown that the frequencies produced by torque oscillations are found to coincide with those produced by air gap eccentricities and electrical rotor faults when the load oscillates synchronous to the rotor position which occurs in reciprocating compressors. In [8], both the voltage and current space vectors are monitored to detect mixed air gap eccentricities in voltage source inverter driven induction motors and artificial neural network techniques are used to extend this to a wide range of operating speeds. Reference [12] uses the frequency spectrum of the three phase stator currents, to detect and estimate the level of static eccentricity based on the normalized magnitudes of the negative sequence frequency components and to separate the effects of load torque oscillations. The instantaneous complex apparent power is used to detect mixed air gap eccentricities in [13]. The torque oscillations at rotational frequency produced as a result of the mixed eccentricity are shown to appear in the complex apparent power and the amplitude of the signatures is shown to increase with severity of the fault. In [14], the pulsed excitation of the machine windings caused by any PWM method in closed-loop drives is used to determine the value of the transient inductances which in turn is used to detect and track the position of the eccentricity.

1.3 Research objectives

The objective of this thesis is to develop a new diagnostic method to detect static and dynamic air gap eccentricities in DFIGs that are run in closed-loop for stator real and reactive power control. The proposed technique will also be able to isolate eccentric faults from stator voltage unbalances and torque oscillations which produce similar signatures in the stator current spectrum. Modified Winding Function Theory (MWFT) [15] will be used to develop a model of an DFIG operating with a static or dynamic eccentricity in the air gap. A different reference frame will be used to decouple the flux equations of the eccentric machine and build a model of the machine in MATLAB®. Simulations will be used to study the effects of the faults on closed-loop stator power controlled DFIG using the developed model. A modification in the existing control scheme will be proposed to enable detection and isolation of the faults. The effectiveness of the proposed control will be supported by simulations and preliminary experimental results.

1.4 Thesis outline

This thesis is organized into four chapters. The first chapter presents an overview of the different topologies used in wind energy conversion systems and a review of the various techniques employed in fault diagnosis of induction machines with emphasis on eccentricity faults. The second chapter derives the equations for stator flux oriented control of a DFIG and proceeds to use MWFT to model the eccentricity. In the third chapter, a new reference frame is used to decouple the flux equations and build the machine model in MATLAB®. A modification in the control to enable eccentricity

detection is proposed and discussed. In the final chapter, a description of the layout of the simulation and experimental set-up is presented and the results from the simulation and experiment are provided and discussed in detail.

2. ANALYSIS OF DFIG UNDER ECCENTRIC CONDITIONS

2.1 Modeling a wind turbine

The primary function of a wind turbine is to convert the kinetic energy of the wind to rotational energy of the blades. The efficiency of this conversion, called the aerodynamic efficiency (C_p), depends on the design of the turbine blades, wind speed, rotor speed and blade pitch. The pitch of the blade defines the angle of attack of the wind on the blade and hence controls the amount of power absorbed.

The power of a mass flow rate (m) of air travelling at a velocity (v) is given by

$$P_{air} = \frac{1}{2} m v^2 \tag{2.1}$$

The mass flow rate (m) of air is given by

$$m = \rho A v \tag{2.2}$$

ρ = air density

A = area of the air mass

The aerodynamic efficiency (C_p) is the fraction of this power that is transferred to the blades and is given by

$$C_p = \frac{P_o}{P_{air}} \tag{2.3}$$

where P_o is the power transferred to the turbine blades.

For a particular turbine design C_p is a function of the tip speed ratio (λ) and the pitch angle (β). The tip speed ratio is given by

$$\lambda = \frac{\omega R}{v} \tag{2.4}$$

ω = angular speed of the turbine

R = radius of the turbine blade

From (2.1) - (2.3) the power transferred to the turbine is given by

$$P_o = 0.5\rho A C_p v^3 \tag{2.5}$$

For a given wind speed and wind turbine configuration, the only variable in the above equation is C_p. The variation of C_p with λ can be obtained from actual measurements. A typical aerodynamic efficiency characteristic is obtained from [16] and shown in Fig. 4. It can be seen that C_p is maximum for an optimal value of λ.

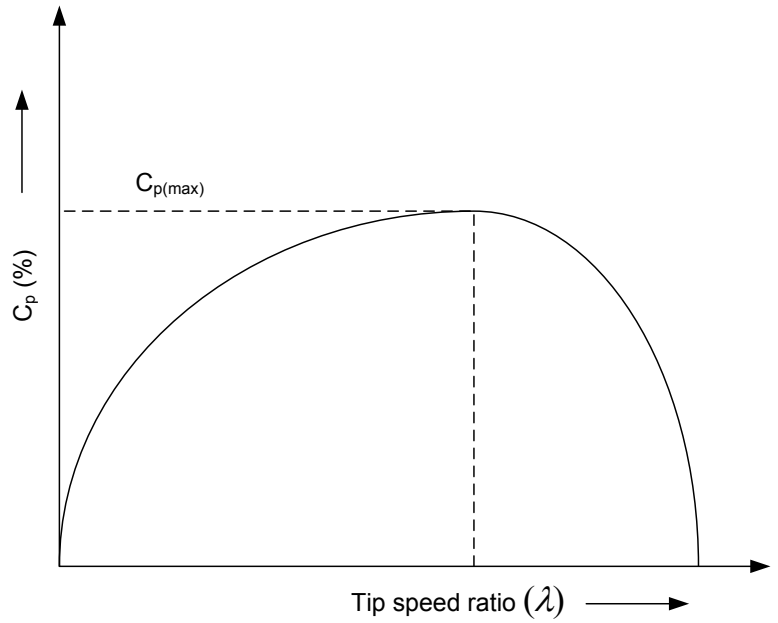

Fig. 4. Variation of aerodynamic efficiency with tip speed ratio

Since λ varies with wind speed, for every wind speed there is a certain λ and hence a certain turbine speed for which the aerodynamic efficiency and hence the power transferred (P_o) is maximum. In fixed speed wind energy conversion systems, the power transferred to the turbine is maximum at a particular wind speed which is defined as the rated wind speed for that system. However for variable speed wind energy conversion systems like DFIG systems the turbine speed is allowed to vary with the wind speed to maintain λ at an optimal value corresponding to maximum C_p thus ensuring maximum efficiency operation at a wide range of wind speeds. This is also called peak power tracking operation [16]. In DFIGs this speed range is dictated by the power rating of the rotor side converter. The operating characteristics for a DFIG based wind energy conversion system is shown in Fig. 5 [16]. It can be seen that shaft speeds of less than *0.7pu* which corresponds to a wind speed of less than $V_1 m/s$ no power is delivered to the grid and the rotor side converter is shut down.

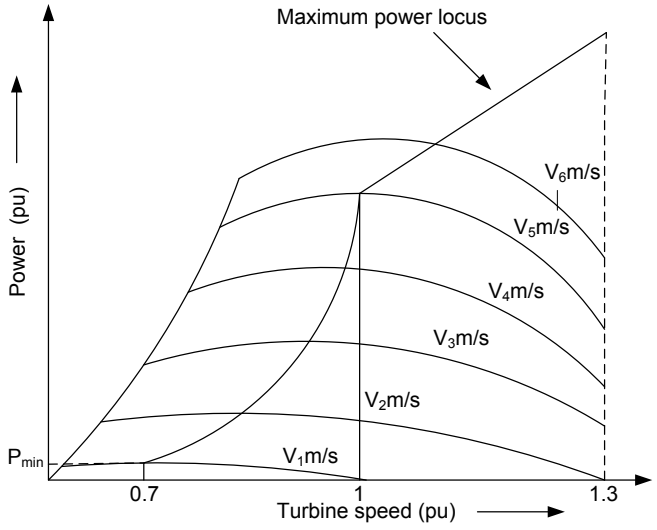

Fig. 5. Operating characteristics of a DFIG based wind turbine generator

When the wind speed crosses $V_1 m/s$ the DFIG is operated in peak power tracking mode, the turbine is accelerated to speed corresponding to the maximum power locus and the stator power command is fixed based on the turbine power characteristics. Above the synchronous speed the maximum power locus is a straight line. When the wind speed exceeds $V_6 m/s$, the power rating of the rotor side converter is exceeded and the turbine moves into pitch control mode to regulate the rotor speed within *1.3pu*. So for the above characteristic, since the rotor handles only the slip power, the rating of the rotor side converter is *0.3P* where *P* is the rated power of the generator.

2.2 Operation of a DFIG

A doubly-fed induction machine is obtained when a bidirectional power converter is connected to the rotor circuit of a wound rotor induction machine. The rotor side converter has two controlled stages to enable bi-directional power flow. A layout of the system is shown in Fig. 6.

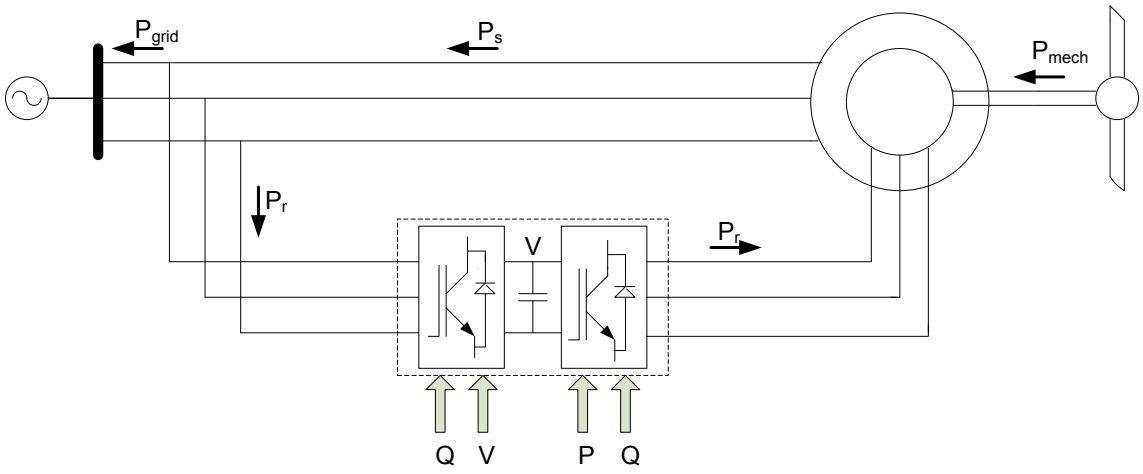

Fig. 6. Block diagram showing the power flow in a DFIG used for wind turbines

The grid side power converter is used to maintain the DC bus at a constant voltage level and the rotor side converter is used to control the real and reactive power injected into the stator. A part of the power supplied by the stator of the DFIG is drawn by the power converter connected to the rotor. So the net power supplied to the grid is P_s – P_r.

Unlike a cage induction machine a DFIG has two motoring and two generating modes of operations. Since electrical power is fed to the rotor circuit, generating operation is possible below the synchronous speed or in the sub-synchronous region and above synchronous speed or super-synchronous region. The two generating modes of operation are discussed below.

When the DFIG operates below synchronous speed, slip power and mechanical power have to be fed to the rotor. As a result the electrical power supplied to the grid for a machine with a power rating of P_s is $(1-s)P_s$ of which sP_s is drawn by the rotor circuit. When the DFIG operates in the super-synchronous region, the torque is maintained at rated value and the slip power is recovered through the rotor circuit. So the power supplied to the grid is $(1+s)P_s$ of which sP_s is supplied through the rotor converters. The power flow diagram for the two generating modes is shown in Fig. 7.

When the input mechanical power is below P_{min}, shown in Fig. 5 the DFIG is operated in speed control mode and the rotor speed is maintained at $0.7pu$. When the input power exceeds P_{min} the DFIG is operated in maximum power tracking mode and the rotor is allowed to accelerate to the speed corresponding to the maximum power locus. At synchronous speed the torque is at its rated value.

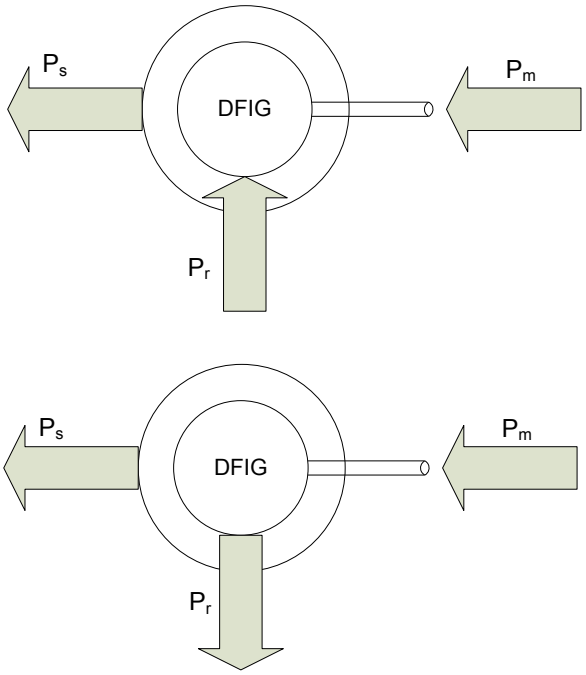

Fig. 7. Power flow for generating modes of operation of a DFIG

If the mechanical torque is increased so that the rotor accelerates to a speed range of *1pu* to *1.3pu* the DFIG is operated at constant rated torque with slip power recovery through the rotor circuit. For wind speeds higher than this, pitch control is used to restrict the rotor speed to *1.3pu*. Since the bidirectional rotor side converter handles only the slip power it is rated at 30% of the rated power output of the generator.

2.3 Modeling a DFIG

The coupled circuit model is used to obtain the equations of a DFIG. For a sinusoidal full pitched winding distribution, the self and mutual inductances can be obtained using winding function approach as

$$L_{aa} = \frac{\mu_o \pi r l}{g}\left(\frac{N_t}{P}\right)^2 \tag{2.6}$$

$$L_{ab} = \frac{\mu_o \pi r l}{g}\left(\frac{N_t}{P}\right)^2 \cos(\theta_r) \tag{2.7}$$

μ_0 = permeability of air

g = air gap length

l = length of stator/rotor

r = radius of stator/rotor

N_t = number of turns of windings a and b

θ_r = Angular separation between windings a and b

P = number of poles in windings a and b

The stator and rotor voltages can be expressed in matrix form as

$$v_{abcs} = r_s i_{abcs} + p\lambda_{abcs} \tag{2.8}$$

$$v_{abcr} = r_r i_{abcr} + p\lambda_{abcr} \tag{2.9}$$

The flux equations for the three stator and three rotor windings is given by

$$\lambda_{abcs} = L_{abcs} i_{abcs} + L_{abcsr} i_{abcr} \tag{2.10}$$

$$\lambda_{abcr} = L_{abcrs} i_{abcs} + L_{abcr} i_{abcr} \tag{2.11}$$

The inductance matrices are obtained from (2.6) and (2.7) for N_s turns on the stator and N_r turns on the rotor.

$$L_{abcs} = \begin{bmatrix} L_{ls} + L_{ss} & -\frac{1}{2}L_{ss} & -\frac{1}{2}L_{ss} \\ -\frac{1}{2}L_{ss} & L_{ls} + L_{ss} & -\frac{1}{2}L_{ss} \\ -\frac{1}{2}L_{ss} & -\frac{1}{2}L_{ss} & L_{ls} + L_{ss} \end{bmatrix} \tag{2.12}$$

$$L_{abcsr} = \begin{bmatrix} L_m \cos\theta_r & L_m \cos\left(\theta_r + \frac{2\pi}{3}\right) & L_m \cos\left(\theta_r - \frac{2\pi}{3}\right) \\ L_m \cos\left(\theta_r - \frac{2\pi}{3}\right) & L_m \cos\theta_r & L_m \cos\left(\theta_r + \frac{2\pi}{3}\right) \\ L_m \cos\left(\theta_r + \frac{2\pi}{3}\right) & L_m \cos\left(\theta_r - \frac{2\pi}{3}\right) & L_m \cos\theta_r \end{bmatrix} \tag{2.13}$$

$$L_{abcrs} = \begin{bmatrix} L_m \cos\theta_r & L_m \cos\left(\theta_r - \frac{2\pi}{3}\right) & L_m \cos\left(\theta_r + \frac{2\pi}{3}\right) \\ L_m \cos\left(\theta_r + \frac{2\pi}{3}\right) & L_m \cos\theta_r & L_m \cos\left(\theta_r - \frac{2\pi}{3}\right) \\ L_m \cos\left(\theta_r - \frac{2\pi}{3}\right) & L_m \cos\left(\theta_r + \frac{2\pi}{3}\right) & L_m \cos\theta_r \end{bmatrix} \tag{2.14}$$

$$L_{abcs} = \begin{bmatrix} L_{lr} + L_{rr} & -\frac{1}{2}L_{rr} & -\frac{1}{2}L_{rr} \\ -\frac{1}{2}L_{rr} & L_{lr} + L_{rr} & -\frac{1}{2}L_{rr} \\ -\frac{1}{2}L_{rr} & -\frac{1}{2}L_{rr} & L_{lr} + L_{rr} \end{bmatrix} \tag{2.15}$$

where,

$$L_{sm} = \frac{\mu_o \pi r l}{g}\left(\frac{N_s}{P}\right)^2$$

$$L_{rm} = \frac{\mu_o \pi r l}{g}\left(\frac{N_r}{P}\right)^2$$

$$L_m = \frac{\mu_o \pi r l}{g}\left(\frac{N_s}{P}\right)\left(\frac{N_r}{P}\right)$$

L_{ls} and L_{lr} = Leakage inductances of stator and rotor

To reduce the complexity and enable decoupled control of torque and flux the machine equations are transformed to a reference frame that is attached to stator flux.

This reference frame is thus rotating at the synchronous speed of $\theta_e = \omega_e t$. Here $\omega_e = 2\pi f$ where f is the frequency of the stator currents/voltages. This means that at steady state all stator variables have constant DC values. A synchronous frame for the rotor would be a frame rotating at a speed of $\omega_e - \omega_r$ when placed on the rotor of the machine (in the same direction). So for an outside observer this frame is rotating at synchronous speed. A vector diagram illustrating the abc and dq frames is shown in Fig. 8. The transformation matrices to transform from abc to synchronous dq frame and back are given by [17]

$$\left[T_{qd}(\theta_e)\right] = \frac{2}{3}\begin{bmatrix} \cos\theta_e & \cos\left(\theta_e - \frac{2\pi}{3}\right) & \cos\left(\theta_e + \frac{2\pi}{3}\right) \\ \sin\theta_e & \sin\left(\theta_e - \frac{2\pi}{3}\right) & \sin\left(\theta_e + \frac{2\pi}{3}\right) \\ \frac{1}{2} & \frac{1}{2} & \frac{1}{2} \end{bmatrix} \tag{2.16}$$

$$\left[T_{qd}(\theta_e)\right]^{-1} = \begin{bmatrix} \cos\theta_e & \sin\theta_e & 1 \\ \cos\left(\theta_e - \frac{2\pi}{3}\right) & \sin\left(\theta_e - \frac{2\pi}{3}\right) & 1 \\ \cos\left(\theta_e + \frac{2\pi}{3}\right) & \sin\left(\theta_e + \frac{2\pi}{3}\right) & 1 \end{bmatrix} \tag{2.17}$$

Applying the transformation to stator voltage equation (2.8)

$$v_{qds} = r_s i_{dqs} + \left[T_{qd}(\theta_e)\right] p\left[T_{qd}(\theta_e)\right]^{-1} \lambda_{qds} \tag{2.18}$$

$$v_{qds} = r_s i_{dqs} + \left[T_{qd}(\theta_e)\right]\left(p\left[T_{qd}(\theta_e)\right]^{-1} \frac{d\theta_e}{dt} \lambda_{qds} + \left[T_{qd}(\theta_e)\right]^{-1} p\lambda_{qds} \right) \tag{2.19}$$

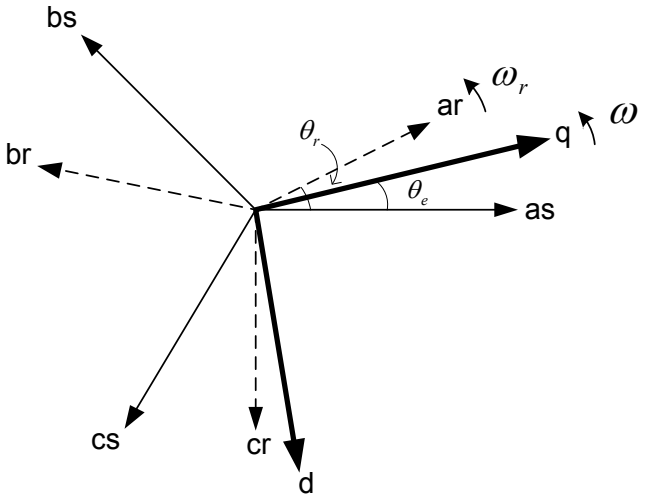

Fig. 8. Vector diagram showing the abc and synchronous dq reference frames

$$v_{qds} = r_s i_{dqs} + \omega_e \begin{bmatrix} 0 & 1 & 0 \\ -1 & 0 & 0 \\ 0 & 0 & 0 \end{bmatrix} \lambda_{qds} + p\lambda_{qds} \tag{2.20}$$

Similarly the rotor voltage equation (2.9) is transformed as follows

$$v_{qdr} = r_r i_{dqr} + \left[T_{qd}(\theta_e - \theta_r)\right] p \left[T_{qd}(\theta_e - \theta_r)\right]^{-1} \lambda_{qdr} \tag{2.21}$$

$$v_{qdr} = r_r i_{dqr} + \left(\omega_e - \omega_r\right) \begin{bmatrix} 0 & 1 & 0 \\ -1 & 0 & 0 \\ 0 & 0 & 0 \end{bmatrix} \lambda_{qdr} + p\lambda_{qdr} \tag{2.22}$$

Applying the transformation to the flux linkage equations (2.10) and (2.11)

$$\lambda_{qds} = \left[T_{qd}(\theta_e)\right] L_{abcs} \left[T_{qd}(\theta_e)\right]^{-1} i_{qds} + \left[T_{qd}(\theta_e)\right] L_{abcsr} \left[T_{qd}(\theta_e - \theta_r)\right]^{-1} i_{qdr} \tag{2.23}$$

$$\lambda_{qdr} = \left[T_{qd}(\theta_e - \theta_r)\right] L_{abcrs} \left[T_{qd}(\theta_e)\right]^{-1} i_{qds} + \left[T_{qd}(\theta_e - \theta_r)\right] L_{abcr} \left[T_{qd}(\theta_e - \theta_r)\right]^{-1} i_{qdr} \tag{2.24}$$

Substituting for the inductance matrices from (2.12) - (2.15)

$$\lambda_{qds} = \begin{bmatrix} L_{ls} + \frac{3}{2}L_{ss} & 0 & 0 \\ 0 & L_{ls} + \frac{3}{2}L_{ss} & 0 \\ 0 & 0 & L_{ls} \end{bmatrix} i_{qds} + \begin{bmatrix} \frac{3}{2}L_m & 0 & 0 \\ 0 & \frac{3}{2}L_m & 0 \\ 0 & 0 & 0 \end{bmatrix} i_{qdr} \tag{2.25}$$

$$\lambda_{qdr} = \begin{bmatrix} \frac{3}{2}L_m & 0 & 0 \\ 0 & \frac{3}{2}L_m & 0 \\ 0 & 0 & 0 \end{bmatrix} i_{qds} + \begin{bmatrix} L_{lr} + \frac{3}{2}L_{rr} & 0 & 0 \\ 0 & L_{lr} + \frac{3}{2}L_{rr} & 0 \\ 0 & 0 & L_{lr} \end{bmatrix} i_{qdr} \tag{2.26}$$

From (2.26) it can be seen that on moving to a synchronous reference frame all inductance matrices are diagonal which indicates that there is no mutual coupling between the d and q axis fluxes.

To build an equivalent circuit, the rotor variables are referred to the stator side according to the following

$$\begin{aligned} \lambda'_{qdr} &= \frac{N_s}{N_r}\lambda_{qdr} \\ i'_{qdr} &= \frac{N_s}{N_r} i_{qdr} \\ L'_{lr} &= \left(\frac{N_s}{N_r}\right)^2 L_{lr} \\ L_M &= \frac{3}{2}L_{ss} = \frac{3}{2}\frac{N_s}{N_r}L_m = \frac{3}{2}\frac{N_s}{N_r}L_{rr} \end{aligned} \tag{2.27}$$

The ratio of the stator winding turns to the rotor winding turns is also called the turns-ratio of a wound rotor machine. From (2.18) – (2.27) , the equations of a DFIG can be written as:

$$v_{qds} = r_s i_{dqs} + \omega_e \begin{bmatrix} 0 & 1 & 0 \\ -1 & 0 & 0 \\ 0 & 0 & 0 \end{bmatrix} \lambda_{qds} + p\lambda_{qds} \tag{2.28}$$

$$v'_{qdr} = r'_r i'_{qdr} + (\omega_e - \omega_r) \begin{bmatrix} 0 & 1 & 0 \\ -1 & 0 & 0 \\ 0 & 0 & 0 \end{bmatrix} \lambda'_{qdr} + p\lambda'_{qdr} \tag{2.29}$$

$$\lambda_{qds} = (L_{ls} + L_M) i_{qds} + L_M i'_{qdr} \tag{2.30}$$

$$\lambda'_{qdr} = L_M i_{qds} + (L'_{lr} + L_M) i'_{qdr} \tag{2.31}$$

The q and d-axis equivalent circuits of the DFIG can be obtained from the above equations and are shown in Fig. 9.

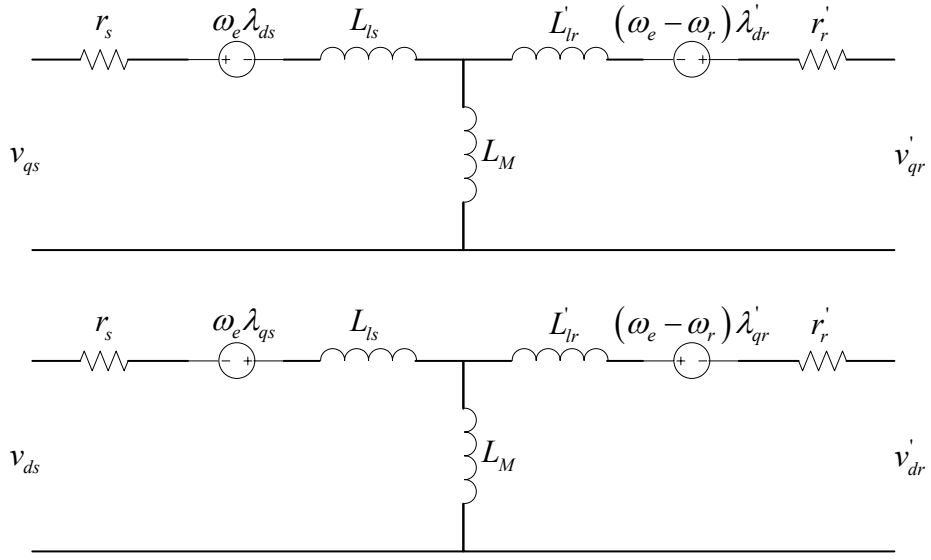

Fig. 9. q and d axis equivalent circuits of the DFIG

2.4 Stator flux oriented control of a DFIG

Stator flux orientation [18] is a convenient way to develop a control scheme for decoupled real and reactive stator power control in a DFIG. The basis of this vector control method is to use the rotor side q and d axis currents to independently control the stator real and reactive power. This is possible in a synchronously rotating reference frame when the stator flux is oriented along the d-axis [19]. The equation for d-axis stator voltage in the stationary d-q frame is given by

$$v_{qds}^{s} = r_s i_{qds}^{s} + p\lambda_{qds}^{s} \tag{2.32}$$

Here the superscript 's' denotes the stationary two axis reference frame. The transformation matrix for this frame can be obtained by setting θ_e = 0 in the transformation matrices given in (2.16) and (2.17). From (2.32) it can be inferred that if the resistive drop across r_s is assumed to be negligible and if λ_{qds} is oriented along the d axis then the stator voltage v_{qds} will be oriented along the q axis.

Since the stator of the DFIG is connected to the grid, the three phase stator voltages can be assumed to be balanced and given by

$$\begin{aligned} v_a &= V_m \cos\left(\omega_e t + \delta\right) \\ v_b &= V_m \cos\left(\omega_e t + \delta - \frac{2\pi}{3}\right) \\ v_c &= V_m \cos\left(\omega_e t + \delta + \frac{2\pi}{3}\right) \end{aligned} \tag{2.33}$$

When this is transformed to the synchronous frame rotating at a speed of ω_e, the d and q axis voltages are given as

$$v_{ds} = -V_m \sin\left(\delta\right) \quad v_{qs} = V_m \cos\left(\delta\right) \tag{2.34}$$

If the stator voltage is oriented along the q axis by assuming a negligible stator resistive drop $v_{ds} = 0$. This means that $\delta = 0$ and $v_{qs} = V_m$. The implication of this is that the synchronous q axis is chosen to be initially aligned with the stator voltage vector at $t = 0$. Also, since flux is now along the d-axis, $\lambda_{qs} = 0$.

2.4.1 Stator angle estimation

For this orientation the stator angle can be found in two ways, using the flux or using the voltage. The vector diagram for estimation of stator angle using the stator voltage is shown in Fig. 10. The stationary q and d-axis components of the stator voltage can be used to estimate the stator angle using the following equation

$$\theta_e = \tan^{-1}\left(-\frac{v_{ds}^s}{v_{qs}^s}\right) \tag{2.35}$$

The negative sign is due to the negative d-axis stator voltage component and ensures that the angle increases in the positive direction from $t = 0$.

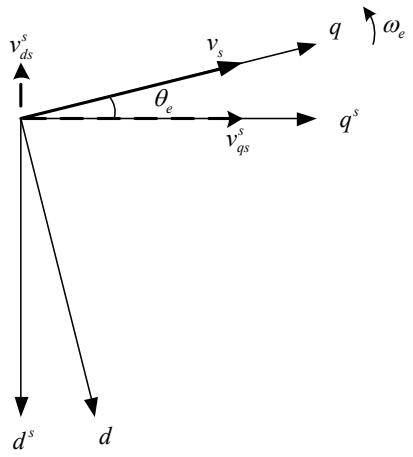

Fig. 10. Stationary and synchronous dq axes with stator voltage orientated along synchronous q axis

2.4.2 Decoupled stator power control

The equations for stator real and reactive power in synchronous d-q frame in terms of stator voltages and currents is given by

$$S = \sqrt{\frac{3}{2}}\left(v_{ds} + jv_{qs}\right).\sqrt{\frac{3}{2}}\left(i_{ds} + ji_{qs}\right)^{*}$$

$$S = \frac{3}{2}\left(v_{ds}i_{ds} + v_{qs}i_{qs}\right) + j\frac{3}{2}\left(v_{qs}i_{ds} - v_{ds}i_{qs}\right)$$

$$P = \frac{3}{2}\left(v_{qs}i_{qs} + v_{ds}i_{ds}\right) \tag{2.36}$$

$$Q = \frac{3}{2}\left(v_{qs}i_{ds} - v_{ds}i_{qs}\right) \tag{2.37}$$

When the stator flux is oriented along the d-axis and the stator is connected to a balanced three-phase bus with peak voltage V_m, as shown in the previous section $v_{ds} = 0$ and $v_{qs} = V_m$. Applying this constraint to the power equation

$$P = \frac{3}{2}V_m i_{qs} \tag{2.38}$$

$$Q = \frac{3}{2}V_m i_{ds} \tag{2.39}$$

From (2.38) and (2.39) it can be seen that the stator real and reactive power can be independently controlled by controlling the q and d-axis components of the stator current. In a DFIG this is achieved by the rotor side converter using a current controlled voltage source inverter.

2.4.3 Control of rotor side converter

From the flux equations in (2.30) and the flux orientation discussed in the previous section, the rotor currents are given by

$$i_{qr} = -\frac{L_s}{L_m} i_{qs} \tag{2.40}$$

$$i_{dr} = \frac{-L_s i_{ds} + \lambda_{ds}}{L_m} \tag{2.41}$$

where

$$L_s = L_{ls} + L_M$$

Using (2.38) - (2.41), the stator real and reactive power can be expressed in terms of the q and d-axis rotor currents.

$$P = -\frac{3}{2}\frac{L_m}{L_s} V_m i_{qr} \tag{2.42}$$

$$Q = \frac{3}{2} V_m \left(\frac{\lambda_{ds} - L_m i_{dr}}{L_s} \right) \tag{2.43}$$

Substituting (2.40) and (2.41) into (2.31)

$$\lambda_{dr}^{'} = \sigma L_r^{'} i_{dr}^{'} + \frac{L_m}{L_s} \lambda_{ds} \tag{2.44}$$

$$\lambda_{qr}^{'} = \sigma L_r^{'} i_{qr}^{'} \tag{2.45}$$

where

$$L_r^{'} = L_{lr}^{'} + L_M$$

$$\sigma = 1 - \frac{L_m^2}{L_s L_r^{'}}$$

Substituting for the rotor flux from (2.44) and (2.45) in (2.29)

$$v_{qr}^{'} = r_r^{'} i_{qr}^{'} + (\omega_e - \omega_r)\sigma L_r^{'} i_{dr}^{'} + (\omega_e - \omega_r)\frac{L_m}{L_s}\lambda_{ds} + \sigma L_r^{'}\frac{di_{qr}^{'}}{dt} \tag{2.46}$$

$$v_{dr}^{'} = r_r^{'} i_{dr}^{'} - (\omega_e - \omega_r)\sigma L_r^{'} i_{qr}^{'} + \sigma L_r^{'}\frac{di_{qr}^{'}}{dt} + \frac{L_m}{L_s}\frac{d\lambda_{ds}}{dt} \tag{2.47}$$

Since the stator of the DFIG is connected to a grid, assuming a stiff bus voltage the stator flux is a constant at steady state and the last term in equation (2.47) becomes zero. The equations also indicate that there is a cross coupling between the q and d-axis rotor voltages. Compensating voltage components have to be applied to decouple the q and d-axis voltages [20]. These are given by

$$v_{qrx}^{'} = (\omega_e - \omega_r)\sigma L_r^{'} i_{dr}^{'} + (\omega_e - \omega_r)\frac{L_m}{L_s}\lambda_{ds} \tag{2.48}$$

$$v_{drx}^{'} = (\omega_e - \omega_r)\sigma L_r^{'} i_{qr}^{'} \tag{2.49}$$

Two PI controllers are used to produce the required rotor voltages and independently control the rotor currents. The coupling voltage terms are compensated by adding the feed-forward compensation terms in (2.48) and (2.49) to the outputs of the PI controllers. A block diagram of the control loop is shown in Fig. 11. The PI controllers can be tuned using pole placement techniques [21] and since the open loop transfer functions are identical, the same gains are used for both controllers.

The closed-loop is a second order unity gain system and the controller gains are given by the following expressions

$$\begin{aligned} K_p &= 2\xi\omega_n\sigma L_r^{'} - r_r^{'} \\ K_i &= \omega_n^2\sigma L_r^{'} \end{aligned} \tag{2.50}$$

where

ξ = damping factor, 1 for critically damped systems

ω_n = natural frequency

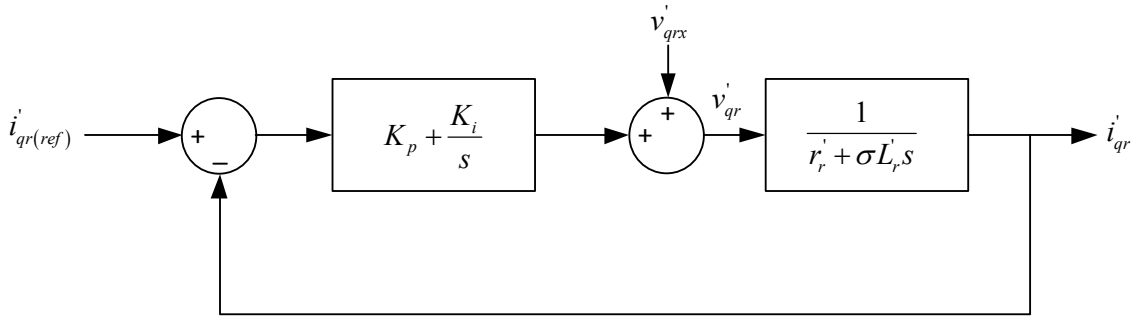

Fig. 11. q-axis inner current loop

The gains are chosen assuming that the system is critically damped and the natural frequency is calculated from the desired settling time (t_s).

An outer control loop is used to obtain the desired rotor current command from the commanded stator power. Since the inner closed-loop is a second order system the overall loop becomes third order when using a first order controller. As a result three controller gains are needed to stabilize the closed-loop by pole placement. However since the inner closed-loop has a unity gain critically damped response, it can be approximated to a first order system with unity gain and a single pole at $-4/t_s$ where t_s is the settling time of the inner closed-loop system [20]. This makes the overall system second order making it possible to stabilize the system using a PI controller. A block diagram of the outer control loop is shown in Fig. 12. Since the stator flux is a constant at steady state assuming a stiff bus voltage the flux term in the expression for reactive

power shown in (2.43) can be considered as a constant disturbance compensated by the integral action in the PI controller.

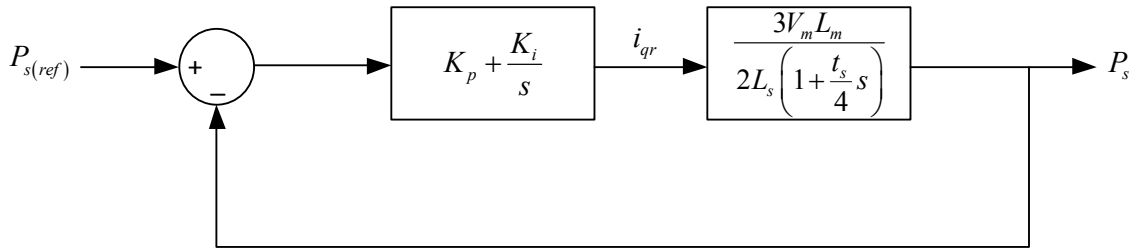

Fig. 12. q-axis outer power loop

So, identical gains can be used for both the outer loop controllers. The expression for the gains of the outer loop controllers is given as follows

$$K_p = \left(\frac{\frac{\xi \omega_n t_s}{2} - 1}{\frac{3}{2} V_m \frac{L_m}{L_s}} \right) \qquad K_i = \left(\frac{\omega_n^2 \frac{t_s}{4}}{\frac{3}{2} V_m \frac{L_m}{L_s}} \right) \tag{2.51}$$

2.4.4 Flux estimation

The stator flux required for providing feed forward compensation is estimated from the stator voltage and current. The flux linkage components in the stationary reference frame are given by

$$\begin{aligned} \lambda_{qs}^s &= \int \left(v_{qs}^s - i_{qs}^s r_s \right) dt \\ \lambda_{ds}^s &= \int \left(v_{ds}^s - i_{ds}^s r_s \right) dt \end{aligned} \tag{2.52}$$

The q and d-axis fluxes can also be used to estimate the stator angle.

2.4.5 Overall control loop

The overall block diagram for controlling the rotor side converter is shown in Fig. 13. The real power command is varied depending on the wind speed for peak power tracking operation. Reactive power command is fixed based on the grid side demand. Current sensors are used to sense the stator and rotor currents and voltage sensors are used to measure the stator voltage. The angular displacement of the rotor θ_r is found using a shaft encoder. The rotor circuit is fed using a current controlled voltage source inverter. The generated rotor voltage reference acts as the modulating signal for switching the legs of the voltage source inverter. Sinusoidal PWM/Space vector PWM can be used to produce the switching sequence.

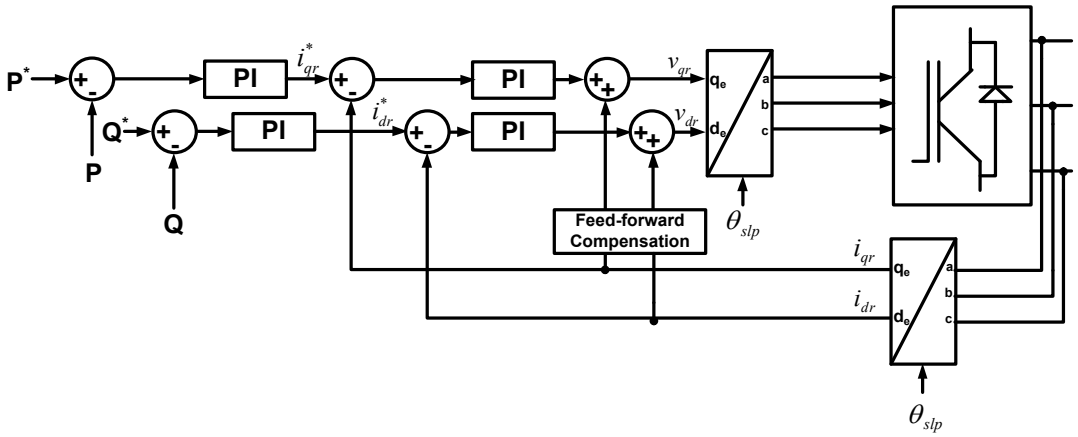

Fig. 13. Control-loop for rotor side converter

2.5 Modified Winding Function Theory (MWFT)

A static eccentricity in the air gap indicates that the center of rotation of the rotor does not coincide with the center of the stator. Coupled magnetic circuit approach can be used to build a model of a DFIG with an eccentricity in the air gap and winding function

theory can be used for estimating the self and mutual inductances of the stator and rotor windings. In the following section a simple system shown in Fig. 14 with single phase windings is used to derive the equations for inductance calculation.

It can be seen from the figure that the air gap under static eccentricity can be defined by the following function [22]

$$g(\phi) = \bar{g}\left(1 + E\cos\phi\right)$$
$$g^{-1}(\phi) = \frac{1}{\bar{g}\sqrt{1-E^2}} - 2\frac{1-\sqrt{1-E^2}}{\bar{g}E\sqrt{1-E^2}}\cos\phi + \ldots = \frac{A_0}{\bar{g}} + \frac{A_1}{\bar{g}}\cos\phi + \ldots \quad (2.53)$$

where

$\bar{g}$ = average length of the air gap

$$\mathrm{E} = \text{relative eccentricity} = \frac{\text{distance between the centers of rotor and stator}}{\text{average air gap length}}$$

Winding function theory can be applied directly to machines with a constant term and even harmonics in the inverse air gap function. However static eccentricity shows the existence of odd harmonics in $g^{-1}(\varphi)$ as seen from (2.53). For analyzing such machines a modification called Modified Winding Function Theory (MWFT) has been introduced in [15].

Consider a system in Fig. 14 that consists of 2 concentric cylinders of ferromagnetic material with infinite permeability and zero conductivity. Both the cylinders have a length of ***l*** and a mean air gap thickness of $\bar{g}$. **r** denotes the outer radius of the rotor.

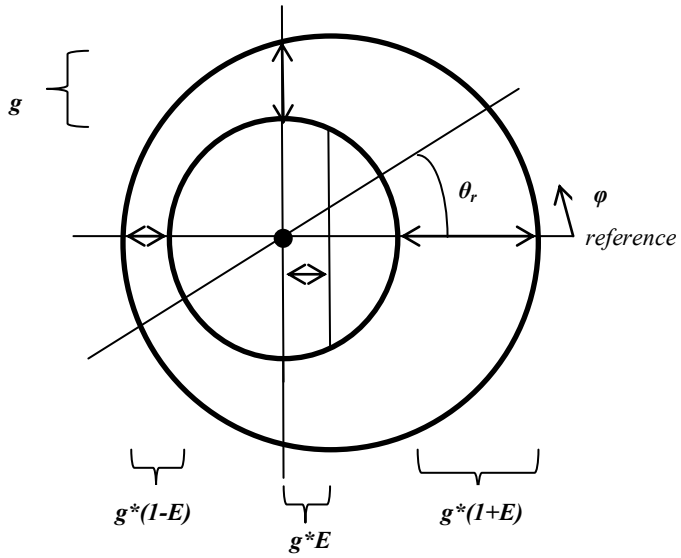

Fig. 14. Machine with static air gap eccentricity. Center of rotor is center of rotation

It is assumed that there are 2 sets of windings A and B on the inner periphery of the outer cylinder. For simplicity the thickness of the winding turns is assumed to be negligible.

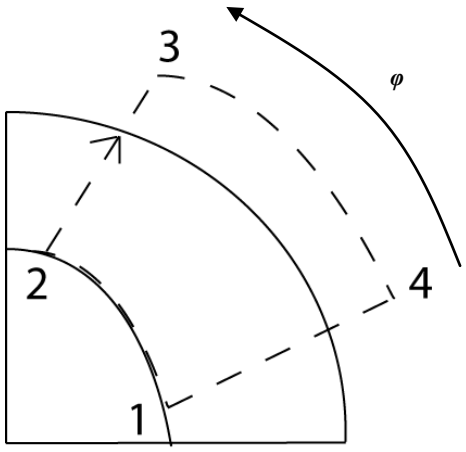

Fig. 15. Ampère an loop with only stator winding

For the loop 1234 shown in Fig. 15, applying Ampere's circuital law assuming only stator winding A is enclosed by the loop.

$$\int_L H.dl = \int_S J.ds$$

If $n(\varphi)$ represents the turns function of the stator winding and all turns carry a uniform current i_A, the above equation reduces to

$$\int H.dl = n(\phi) i_A$$

Assuming that the radial component of the magnetic field is negligible, the axial component of the magnetic field is constant along the air gap and the permeability of iron is infinity, the above equation in terms of MMF along each path in the loop is given by,

$$F_{41}(0) + F_{23}(\phi) = n(\phi) i_A \tag{2.54}$$

where

$$F_{41}(0) = -H(r,0)g(0)$$
$$F_{23}(\phi) = H(r,\phi)g(\phi)$$

Applying Gauss's Law to a cylindrical surface located in the air gap, enclosing the inner cylinder.

$$\int \mu_o H.dA = 0$$

$$\int_0^{2\pi}\int_0^{l} \mu_o H(\phi,r) r.dl.d\phi = 0$$

$$\int_0^{2\pi} H(\phi,r)\, d\phi = 0$$

$$\int_0^{2\pi} \frac{F(\phi)}{g(\phi)} d\phi = 0 \tag{2.55}$$

Dividing by $g(\varphi)$ and integrating (2.54) from 0 to 2π.

$$\int_0^{2\pi} \left(\frac{F_{41}(0)}{g(\phi)} - \frac{F_{23}(\phi)}{g(\phi)} \right) .d\phi = \int_0^{2\pi} \frac{n(\phi)}{g(\phi)} i_A .d\phi \tag{2.56}$$

From (2.55) and (2.56)

$$F_{41}(0) \int_0^{2\pi} \left(\frac{1}{g(\phi)} \right) d\phi = \int_0^{2\pi} n(\phi) g^{-1}(\phi) i_A .d\phi$$

$$F_{41}(0).2\pi.\left\langle g^{-1}(\phi) \right\rangle = \int_0^{2\pi} n(\phi) g^{-1}(\phi) i_A .d\phi \tag{2.57}$$

Here $\langle g^{-1}(\varphi) \rangle$ is the average of the inverse air gap function. From (2.54) and (2.57)

$$F_{23}(\phi) = \left[n(\phi) - \frac{1}{2\pi.\left\langle g^{-1}(\phi) \right\rangle} \int_0^{2\pi} n(\phi) g^{-1}(\phi) d\phi \right] i_A \tag{2.58}$$

The above expression gives the MMF due to the stator winding at any point in the air gap of the machine. The modified winding function is thus given by,

$$M(\phi) = n(\phi) - \frac{1}{2\pi.\left\langle g^{-1}(\phi) \right\rangle} \int_0^{2\pi} n(\phi) g^{-1}(\phi) d\phi \tag{2.59}$$

2.6 Inductance calculation using Modified Winding Function Theory

Consider the machine shown in Fig. 14 with the two sets of windings A and B on the stator. The mutual inductance of B with respect to A is the flux linking winding B due to the current in A. The air gap MMF caused due to the current in winding A can be determined from (2.58) and (2.59) as

$$F_A(\phi) = M_A(\phi) i_A \tag{2.60}$$

The flux in the air gap due to winding A is the product of the MMF and permeance of the air gap. Considering a differential area of cross section $r(d\varphi)l$, the expression for flux is given by,

$$d\Phi = F_A(\phi)\frac{\mu_o r l}{g(\phi)}.d\phi \tag{2.61}$$

The part of this flux linking coil B can be determined by multiplying (2.61) with the turns function of coil B and integrating from 0 to 2π. If $n_B(\varphi)$ denotes the turns function of coil B, then

$$\Phi = \int_0^{2\pi} F_A(\phi) n_B(\phi)\frac{\mu_o r l}{g(\phi)}.d\phi$$

$$\Phi = \mu_o r l \int_0^{2\pi} F_A(\phi) n_B(\phi) g^{-1}(\phi).d\phi \tag{2.62}$$

From (2.60) and(2.62),

$$\Phi = \mu_o r l i_A \int_0^{2\pi} M_A(\phi) n_B(\phi) g^{-1}(\phi).d\phi \tag{2.63}$$

The mutual inductance L_{BA} is obtained by dividing the flux linking B due to the coil A by the current in A.

$$L_{BA} = \mu_o r l \int_0^{2\pi} M_A(\phi) n_B(\phi) g^{-1}(\phi).d\phi \tag{2.64}$$

2.7 Application of MWFT to a DFIG with static eccentricity in the air gap

The equations for inductances developed using MWFT can now be used to derive the flux equations of a DFIG with air gap eccentricity. The procedure for obtaining the inductance matrices is explained in detail for static air gap eccentricity in the following section. The inductance matrices for dynamic air gap eccentricity can be obtained in a similar way. The results obtained for dynamic eccentricity are provided at the end of this chapter.

The air gap function in the presence of static eccentricity as explained earlier is given by

$$\begin{aligned} g(\phi) &= \bar{g}\left(1 + E\cos\phi\right) \\ g^{-1}(\phi) &= \frac{1}{\bar{g}\sqrt{1-E^2}} - 2\frac{1-\sqrt{1-E^2}}{\bar{g}E\sqrt{1-E^2}}\cos\phi + \ldots = \frac{A_0}{\bar{g}} + \frac{A_1}{\bar{g}}\cos\phi + \ldots \end{aligned} \tag{2.65}$$

where

$\bar{g}$ = average length of the air gap

$$\mathrm{E} = \text{relative eccentricity} = \frac{\text{distance between the centers of rotor and stator}}{\text{average air gap length}}$$

The DFIG is assumed to have three phase sinusoidal distributed windings with P poles on the stator and rotor. The spatial angle is φ and the displacement of the A-phase winding of the rotor from the A-phase winding of the stator is $\theta_r=\omega_r t$ where ω_r is the angular speed of the rotor in radians/seconds. For the sake of simplicity it is assumed that both the rotor and the stator windings have identical number of turns N_t. This indicates a unity turns ratio and so rotor variables are unchanged even after being

referred to the stator side. The average radius of the stator/rotor is *r* and the length of stator/rotor is *l*. The turns function for a sinusoidal winding distribution is given by

$$n(\phi) = \frac{N_t}{2}(\cos\phi - 1)$$

Neglecting higher order harmonics the inverse air gap function $g^{-1}(\varphi)$ can be written as (2.65)

$$g^{-1}(\phi) = \frac{A_0}{\bar{g}} + \frac{A_1}{\bar{g}}\cos\phi \tag{2.66}$$

where

$$A_o = \frac{1}{\sqrt{1-E^2}}$$

$$A_1 = -2\frac{1-\sqrt{1-E^2}}{E\sqrt{1-E^2}}$$

The average of the inverse air gap function $\langle g^{-1}(\varphi)\rangle$ is given as

$$\left\langle g^{-1}(\phi)\right\rangle = \frac{A_0}{\bar{g}} \tag{2.67}$$

Taking stator A-phase winding as the spatial reference the turns functions for the three stator phases are given by

$$\begin{aligned} n_{AS}(\phi) &= \frac{N_t}{2}(\cos\phi - 1) \\ n_{BS}(\phi) &= \frac{N_t}{2}\left(\cos\left(\phi - \frac{2\pi}{3}\right) - 1\right) \\ n_{CS}(\phi) &= \frac{N_t}{2}\left(\cos\left(\phi - \frac{4\pi}{3}\right) - 1\right) \end{aligned} \tag{2.68}$$

The turns functions for the rotor windings with respect to the same reference are

$$
\begin{aligned}
n_{AR}(\phi,\theta_r) &= \frac{N_t}{2}\left(\cos(\phi-\theta_r)-1\right)\\
n_{BR}(\phi,\theta_r) &= \frac{N_t}{2}\left(\cos\left(\phi-\theta_r-\frac{2\pi}{3}\right)-1\right)\\
n_{CR}(\phi,\theta_r) &= \frac{N_t}{2}\left(\cos\left(\phi-\theta_r-\frac{4\pi}{3}\right)-1\right)
\end{aligned}
\tag{2.69}
$$

The modified winding function of the three stator and rotor windings is now obtained using (2.59), (2.66), (2.67), (2.68) and (2.69). The equation for inductance in (2.64) is used to calculate the self and mutual inductances of the stator and rotor windings.

$$
\begin{aligned}
M_{AS}(\phi) &= \frac{N_t}{2}\left(\cos(\phi)-\frac{A_1}{2A_0}\right)\\
M_{BS}(\phi) &= \frac{N_t}{2}\left(\cos\left(\phi-\frac{2\pi}{3}\right)-\frac{A_1}{2A_0}\cos\left(\frac{2\pi}{3}\right)\right)\\
M_{CS}(\phi) &= \frac{N_t}{2}\left(\cos\left(\phi-\frac{4\pi}{3}\right)-\frac{A_1}{2A_0}\cos\left(\frac{4\pi}{3}\right)\right)\\
M_{AR}(\phi,\theta_r) &= \frac{N_t}{2}\left(\cos(\phi-\theta_r)-\frac{A_1}{2A_0}\cos(\theta_r)\right)\\
M_{BR}(\phi,\theta_r) &= \frac{N_t}{2}\left(\cos\left(\phi-\left(\theta_r+\frac{2\pi}{3}\right)\right)-\frac{A_1}{2A_0}\cos\left(\theta_r+\frac{2\pi}{3}\right)\right)\\
M_{CR}(\phi,\theta_r) &= \frac{N_t}{2}\left(\cos\left(\phi-\left(\theta_r-\frac{2\pi}{3}\right)\right)-\frac{A_1}{2A_0}\cos\left(\theta_r-\frac{2\pi}{3}\right)\right)
\end{aligned}
\tag{2.70}
$$

The inductance matrices obtained are as follows

$$
L_{abcs} = \begin{bmatrix}
L_{ls}+L_k+L_m & \frac{-1}{2}L_k-\frac{1}{2}L_m & \frac{-1}{2}L_k-\frac{1}{2}L_m\\
\frac{-1}{2}L_k-\frac{1}{2}L_m & L_{ls}+L_k+\frac{1}{4}L_m & \frac{-1}{2}L_k+\frac{1}{4}L_m\\
\frac{-1}{2}L_k-\frac{1}{2}L_m & \frac{-1}{2}L_k+\frac{1}{4}L_m & L_{ls}+L_k+\frac{1}{4}L_m
\end{bmatrix}
\tag{2.71}
$$

$$L_{abcr} = \begin{bmatrix} L_{lr} + L_k + L_m \cos^2\theta_r & \frac{-1}{2}L_k + L_m \cos\theta_r \cos(\theta_r + \frac{2\pi}{3}) & \frac{-1}{2}L_k + L_m \cos\theta_r \cos(\theta_r - \frac{2\pi}{3}) \\ \frac{-1}{2}L_k + L_m \cos\theta_r \cos(\theta_r + \frac{2\pi}{3}) & L_{lr} + L_k + L_m \cos^2(\theta_r + \frac{2\pi}{3}) & \frac{-1}{2}L_k + L_m \cos(\theta_r - \frac{2\pi}{3})\cos(\theta_r + \frac{2\pi}{3}) \\ \frac{-1}{2}L_k + L_m \cos\theta_r \cos(\theta_r - \frac{2\pi}{3}) & \frac{-1}{2}L_k + L_m \cos(\theta_r - \frac{2\pi}{3})\cos(\theta_r + \frac{2\pi}{3}) & L_{lr} + L_k + L_m \cos^2(\theta_r - \frac{2\pi}{3}) \end{bmatrix}$$

(2.72)

$$L_{abcsr} = \begin{bmatrix} L_k \cos\theta_r + L_m \cos\theta_r & L_k \cos(\theta_r + \frac{2\pi}{3}) + L_m \cos(\theta_r + \frac{2\pi}{3}) & L_k \cos(\theta_r - \frac{2\pi}{3}) + L_m \cos(\theta_r - \frac{2\pi}{3}) \\ L_k \cos(\theta_r - \frac{2\pi}{3}) - \frac{1}{2}L_m \cos\theta_r & L_k \cos\theta_r - \frac{1}{2}L_m \cos(\theta_r + \frac{2\pi}{3}) & L_k \cos(\theta_r + \frac{2\pi}{3}) - \frac{1}{2}L_m \cos(\theta_r - \frac{2\pi}{3}) \\ L_k \cos(\theta_r + \frac{2\pi}{3}) - \frac{1}{2}L_m \cos\theta_r & L_k \cos(\theta_r - \frac{2\pi}{3}) - \frac{1}{2}L_m \cos(\theta_r + \frac{2\pi}{3}) & L_k \cos\theta_r - \frac{1}{2}L_m \cos(\theta_r - \frac{2\pi}{3}) \end{bmatrix}$$

(2.73)

$$L_{abcrs} = \begin{bmatrix} L_k \cos\theta_r + L_m \cos\theta_r & L_k \cos(\theta_r - \frac{2\pi}{3}) - \frac{1}{2}L_m \cos\theta_r & L_k \cos(\theta_r + \frac{2\pi}{3}) - \frac{1}{2}L_m \cos\theta_r \\ L_k \cos(\theta_r + \frac{2\pi}{3}) + L_m \cos(\theta_r + \frac{2\pi}{3}) & L_k \cos\theta_r - \frac{1}{2}L_m \cos(\theta_r + \frac{2\pi}{3}) & L_k \cos(\theta_r - \frac{2\pi}{3}) - \frac{1}{2}L_m \cos(\theta_r + \frac{2\pi}{3}) \\ L_k \cos(\theta_r - \frac{2\pi}{3}) + L_m \cos(\theta_r - \frac{2\pi}{3}) & L_k \cos(\theta_r + \frac{2\pi}{3}) - \frac{1}{2}L_m \cos(\theta_r - \frac{2\pi}{3}) & L_k \cos\theta_r - \frac{1}{2}L_m \cos(\theta_r - \frac{2\pi}{3}) \end{bmatrix}$$

(2.74)

where

$$L_k = \frac{\mu_0 \pi r l N_t^{\,2} A_0}{P^2 \overline{g}} \tag{2.75}$$

$$L_m = -\frac{\mu_0 \pi r l N_t^{\,2} A_1^{\,2}}{2P^2 \overline{g} A_0} \tag{2.76}$$

To validate the above results, it can be seen from the inverse air gap function that in the absence of static eccentricity in the air gap, $A_1=0$ and $A_0=1$. When this is applied to the above equations they reduce to equations obtained in (2.12) - (2.15), which were derived for a DFIG with a uniform air gap using winding function theory. As expected

under static eccentricity the stator self-inductance matrix does not have any time varying inductances since for a given point on the stator the air gap is always fixed. To analyze the behavior of an eccentric DFIG operating in closed-loop for stator power control, the complete voltage and flux equations are transformed to the synchronous reference frame.

The voltage equations in the synchronous frame remain unchanged under static eccentricity and are given by

$$v_{qds} = \omega \begin{bmatrix} 0 & 1 & 0 \\ -1 & 0 & 0 \\ 0 & 0 & 0 \end{bmatrix} \lambda_{qds} + p\lambda_{qds} + r_s i_{qds}$$

$$v_{qdr} = (\omega - \omega_r) \begin{bmatrix} 0 & 1 & 0 \\ -1 & 0 & 0 \\ 0 & 0 & 0 \end{bmatrix} \lambda_{qdr} + p\lambda_{qdr} + r_r i_{qdr}$$

Applying transformations to the flux equations in the abc frame

$$\lambda_{qds} = \left[T_{qd}(\theta_e)\right] L_{abcs} \left[T_{qd}(\theta_e)\right]^{-1} i_{qds} + \left[T_{qd}(\theta_e)\right] L_{abcsr} \left[T_{qd}(\theta_e - \theta_r)\right]^{-1} i_{qdr} \qquad (2.77)$$

$$\lambda_{qdr} = \left[T_{qd}(\theta_e - \theta_r)\right] L_{abcrs} \left[T_{qd}(\theta_e)\right]^{-1} i_{qds} + \left[T_{qd}(\theta_e - \theta_r)\right] L_{abcr} \left[T_{qd}(\theta_e - \theta_r)\right]^{-1} i_{qdr} \qquad (2.78)$$

Substituting for the inductance matrices from (2.71) - (2.74), the inductances in the synchronous dq frame are given by

$$\left[T_{qd}(\theta_e)\right] L_{abcs} \left[T_{qd}(\theta_e)\right]^{-1} = \begin{bmatrix} \frac{3}{2}L_k + \frac{3}{2}L_m \cos^2\theta_e + L_{ls} & \frac{3}{2}L_m \cos\theta_e \sin\theta_e & 0 \\ \frac{3}{2}L_m \cos\theta_e \sin\theta_e & \frac{3}{2}L_k + \frac{3}{2}L_m \sin^2\theta_e + L_{ls} & 0 \\ 0 & 0 & L_{ls} \end{bmatrix} \qquad (2.79)$$

$$\left[T_{qd}(\theta_e)\right]L_{abcsr}\left[T_{qd}(\theta_e-\theta_r)\right]^{-1}=\begin{bmatrix}\frac{3}{2}L_k+\frac{3}{2}L_m\cos^2\theta_e & \frac{3}{2}L_m\cos\theta_e\sin\theta_e & 0\\ \frac{3}{2}L_m\cos\theta_e\sin\theta_e & \frac{3}{2}L_k+\frac{3}{2}L_m\sin^2\theta_e & 0\\ 0 & 0 & 0\end{bmatrix} \quad (2.80)$$

$$\left[T_{qd}(\theta_e-\theta_r)\right]L_{abcrs}\left[T_{qd}(\theta_e)\right]^{-1}=\begin{bmatrix}\frac{3}{2}L_k+\frac{3}{2}L_m\cos^2\theta_e & \frac{3}{2}L_m\cos\theta_e\sin\theta_e & 0\\ \frac{3}{2}L_m\cos\theta_e\sin\theta_e & \frac{3}{2}L_k+\frac{3}{2}L_m\sin^2\theta_e & 0\\ 0 & 0 & 0\end{bmatrix} \quad (2.81)$$

$$\left[T_{qd}(\theta_e-\theta_r)\right]L_{abcr}\left[T_{qd}(\theta_e-\theta_r)\right]^{-1}=\begin{bmatrix}\frac{3}{2}L_k+\frac{3}{2}L_m\cos^2\theta_e+L_{lr} & \frac{3}{2}L_m\cos\theta_e\sin\theta_e & 0\\ \frac{3}{2}L_m\cos\theta_e\sin\theta_e & \frac{3}{2}L_k+\frac{3}{2}L_m\sin^2\theta_e+L_{lr} & 0\\ 0 & 0 & L_{lr}\end{bmatrix} \quad (2.82)$$

From (2.77) - (2.82), the stator and rotor flux equations for a DFIG with static eccentricity in the air gap are

$$\lambda_{qs}=(L_{ls}+\frac{3}{2}L_k+\frac{3}{2}L_m\cos^2\theta_e)i_{qs}+(\frac{3}{2}L_m\cos\theta_e\sin\theta_e)i_{ds}+(\frac{3}{2}L_k+\frac{3}{2}L_m\cos^2\theta_e)i_{qr}+(\frac{3}{2}L_m\cos\theta_e\sin\theta_e)i_{dr} \quad (2.83)$$

$$\lambda_{ds}=(\frac{3}{2}L_m\cos\theta_e\sin\theta_e)i_{qs}+(L_{ls}+\frac{3}{2}L_k+\frac{3}{2}L_m\sin^2\theta_e)i_{ds}+(\frac{3}{2}L_m\cos\theta_e\sin\theta_e)i_{qr}+(\frac{3}{2}L_k+\frac{3}{2}L_m\sin^2\theta_e)i_{dr} \quad (2.84)$$

$$\lambda_{qr}=(\frac{3}{2}L_k+\frac{3}{2}L_m\cos^2\theta_e)i_{qs}+(\frac{3}{2}L_m\cos\theta_e\sin\theta_e)i_{ds}+(L_{lr}+\frac{3}{2}L_k+\frac{3}{2}L_m\cos^2\theta_e)i_{qr}+(\frac{3}{2}L_m\cos\theta_e\sin\theta_e)i_{dr} \quad (2.85)$$

$$\lambda_{dr} = (\frac{3}{2}L_m \cos\theta_e \sin\theta_e)i_{qs} + (\frac{3}{2}L_k + \frac{3}{2}L_m \sin^2\theta_e)i_{ds} + (\frac{3}{2}L_m \cos\theta_e \sin\theta_e)i_{qr} + (L_{lr} + \frac{3}{2}L_k + \frac{3}{2}L_m \sin^2\theta_e)i_{dr} \tag{2.86}$$

From (2.83) - (2.86), static air gap eccentricity introduces a mutual coupling between the d and q axis fluxes in the synchronous frame when compared to a healthy machine equations in (2.30) and (2.31). The synchronous frame flux equations also have time varying inductance components. If a stiff grid voltage is applied to the stator of a DFIG, the stator voltage term in the synchronous reference frame will have a constant DC value. So the time varying inductance terms oscillating at twice the stator frequency, *2f (2ω_e)*, will induce the same oscillations in the synchronous frame stator and rotor currents, resulting in a torque oscillations at twice the synchronous frequency. The oscillations are also present in the stator real and reactive power as seen from (2.38) and (2.39).

2.8 Extension of results to dynamic air gap eccentricities

In the presence of a dynamic eccentricity in the air gap the center of rotation of the rotor moves around the center of the stator. As a result, unlike static eccentricities, the position of minimum air gap also rotates around the stator as the rotor rotates. This introduces a rotor speed dependence in the air gap function. The air gap function for DFIGs with dynamic air gap eccentricities is given by [22]

$$\begin{aligned} g(\phi) &= \bar{g}\left(1 + E\cos(\phi - \theta_r)\right) \\ g^{-1}(\phi) &= \frac{1}{\bar{g}\sqrt{1-E^2}} - 2\frac{1-\sqrt{1-E^2}}{\bar{g}E\sqrt{1-E^2}}\cos(\phi-\theta_r) + \ldots = \frac{A_0}{\bar{g}} + \frac{A_1}{\bar{g}}\cos(\phi-\theta_r) + \ldots \end{aligned} \tag{2.87}$$

The Fig. 16 shows a dynamic eccentricity in the air gap of an electrical machine.

Using the turns functions for the stator and rotor windings from (2.68) and (2.69), the modified winding functions are obtained from (2.59). The equation for inductance in (2.64) is used to calculate the self and mutual inductances of the stator and rotor windings.

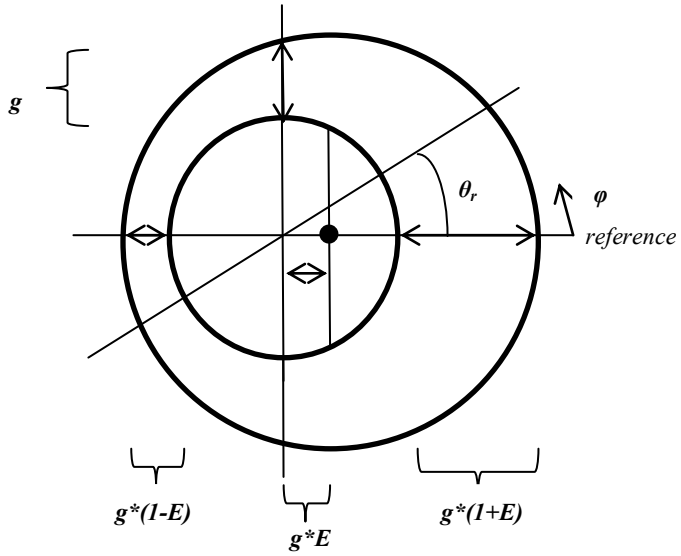

Fig. 16. Machine with dynamic air gap eccentricity. Center of stator is center of rotation

The inductance matrices under dynamic eccentricity are as follows. The notations used are the same as those introduced for static eccentricity.

$$L_{abcs} = \begin{bmatrix} L_{ls} + L_k + L_m \cos^2\theta_r & -\frac{1}{2}L_k + L_m \cos\theta_r \cos(\theta_r - \frac{2\pi}{3}) & -\frac{1}{2}L_k + L_m \cos\theta_r \cos(\theta_r + \frac{2\pi}{3}) \\ -\frac{1}{2}L_k + L_m \cos\theta_r \cos(\theta_r - \frac{2\pi}{3}) & L_{ls} + L_k + L_m \cos^2(\theta_r - \frac{2\pi}{3}) & -\frac{1}{2}L_k + L_m \cos(\theta_r + \frac{2\pi}{3})\cos(\theta_r - \frac{2\pi}{3}) \\ -\frac{1}{2}L_k + L_m \cos\theta_r \cos(\theta_r + \frac{2\pi}{3}) & -\frac{1}{2}L_k + L_m \cos(\theta_r + \frac{2\pi}{3})\cos(\theta_r - \frac{2\pi}{3}) & L_{ls} + L_k + L_m \cos^2(\theta_r + \frac{2\pi}{3}) \end{bmatrix} \quad (2.88)$$

$$L_{abcsr}=\begin{bmatrix} L_k\cos\theta_r+L_m\cos\theta_r & L_k\cos(\theta_r+\frac{2\pi}{3})-\frac{L_m}{2}\cos\theta_r & L_k\cos(\theta_r-\frac{2\pi}{3})-\frac{L_m}{2}\cos\theta_r \\ L_k\cos(\theta_r-\frac{2\pi}{3})+L_m\cos(\theta_r-\frac{2\pi}{3}) & L_k\cos\theta_r-\frac{1}{2}L_m\cos(\theta_r-\frac{2\pi}{3}) & L_k\cos(\theta_r+\frac{2\pi}{3})-\frac{1}{2}L_m\cos(\theta_r-\frac{2\pi}{3}) \\ L_k\cos(\theta_r+\frac{2\pi}{3})+L_m\cos(\theta_r+\frac{2\pi}{3}) & L_k\cos(\theta_r-\frac{2\pi}{3})-\frac{1}{2}L_m\cos(\theta_r+\frac{2\pi}{3}) & L_k\cos\theta_r-\frac{1}{2}L_m\cos(\theta_r+\frac{2\pi}{3}) \end{bmatrix}$$

(2.89)

$$L_{abcrs}=\begin{bmatrix} L_k\cos\theta_r+L_m\cos\theta_r & L_k\cos(\theta_r-\frac{2\pi}{3})+L_m\cos(\theta_r-\frac{2\pi}{3}) & L_k\cos(\theta_r+\frac{2\pi}{3})+L_m\cos(\theta_r+\frac{2\pi}{3}) \\ L_k\cos(\theta_r+\frac{2\pi}{3})-\frac{1}{2}L_m\cos\theta_r & L_k\cos\theta_r-\frac{1}{2}L_m\cos(\theta_r-\frac{2\pi}{3}) & L_k\cos(\theta_r-\frac{2\pi}{3})-\frac{1}{2}L_m\cos(\theta_r+\frac{2\pi}{3}) \\ L_k\cos(\theta_r-\frac{2\pi}{3})-\frac{1}{2}L_m\cos\theta_r & L_k\cos(\theta_r+\frac{2\pi}{3})-\frac{1}{2}L_m\cos(\theta_r-\frac{2\pi}{3}) & L_k\cos\theta_r-\frac{1}{2}L_m\cos(\theta_r+\frac{2\pi}{3}) \end{bmatrix}$$

(2.90)

$$L_{abcrr}=\begin{bmatrix} L_{lr}+L_k+L_m & -\frac{1}{2}L_k-\frac{1}{2}L_m & -\frac{1}{2}L_k-\frac{1}{2}L_m \\ -\frac{1}{2}L_k-\frac{1}{2}L_m & L_{lr}+L_k+\frac{1}{4}L_m & -\frac{1}{2}L_k+\frac{1}{4}L_m \\ -\frac{1}{2}L_k-\frac{1}{2}L_m & -\frac{1}{2}L_k+\frac{1}{4}L_m & L_{lr}+L_k+\frac{1}{4}L_m \end{bmatrix} \quad (2.91)$$

Similar to the previous case, to validate the above results, $A_1=0$ and $A_0=1$. When this is applied to the above equations they reduce to the equations obtained in (2.12) - (2.15), which were derived for a DFIG with a uniform air gap using winding function theory. As expected, under dynamic eccentricity the rotor self-inductance matrix does not have any time varying inductances since for a given point on the rotor the air gap is always fixed and the point of minimum air gap moves with the rotor. The voltage equations of a DFIG with dynamic eccentricity in the air gap in synchronous reference frame are identical to those of a healthy machine. The flux equations are obtained by transforming the (2.30) and (2.31) to the synchronous frames using the inductance matrices derived in (2.88) - (2.91).

$$\left[T_{qd}(\theta_e)\right]L_{abcs}\left[T_{qd}(\theta_e)\right]^{-1}=\begin{bmatrix}\frac{3}{2}L_k+\frac{3}{2}L_m\cos^2(\theta_e-\theta_r)+L_{ls} & \frac{3}{2}L_m\cos(\theta_e-\theta_r)\sin(\theta_e-\theta_r) & 0\\ \frac{3}{2}L_m\cos(\theta_e-\theta_r)\sin(\theta_e-\theta_r) & \frac{3}{2}L_k+\frac{3}{2}L_m\sin^2(\theta_e-\theta_r)+L_{ls} & 0\\ 0 & 0 & L_{ls}\end{bmatrix}$$

(2.92)

$$\left[T_{qd}(\theta_e)\right]L_{abcsr}\left[T_{qd}(\theta_e-\theta_r)\right]^{-1}=\begin{bmatrix}\frac{3}{2}L_k+\frac{3}{2}L_m\cos^2(\theta_e-\theta_r) & \frac{3}{2}L_m\cos(\theta_e-\theta_r)\sin(\theta_e-\theta_r) & 0\\ \frac{3}{2}L_m\cos(\theta_e-\theta_r)\sin(\theta_e-\theta_r) & \frac{3}{2}L_k+\frac{3}{2}L_m\sin^2(\theta_e-\theta_r) & 0\\ 0 & 0 & 0\end{bmatrix}$$

(2.93)

$$\left[T_{qd}(\theta_e-\theta_r)\right]L_{abcrs}\left[T_{qd}(\theta_e)\right]^{-1}=\begin{bmatrix}\frac{3}{2}L_k+\frac{3}{2}L_m\cos^2(\theta_e-\theta_r) & \frac{3}{2}L_m\cos(\theta_e-\theta_r)\sin(\theta_e-\theta_r) & 0\\ \frac{3}{2}L_m\cos(\theta_e-\theta_r)\sin(\theta_e-\theta_r) & \frac{3}{2}L_k+\frac{3}{2}L_m\sin^2(\theta_e-\theta_r) & 0\\ 0 & 0 & 0\end{bmatrix}$$

(2.94)

$$\left[T_{qd}(\theta_e-\theta_r)\right]L_{abcr}\left[T_{qd}(\theta_e-\theta_r)\right]^{-1}=\begin{bmatrix}\frac{3}{2}L_k+\frac{3}{2}L_m\cos^2(\theta_e-\theta_r)+L_{lr} & \frac{3}{2}L_m\cos(\theta_e-\theta_r)\sin(\theta_e-\theta_r) & 0\\ \frac{3}{2}L_m\cos(\theta_e-\theta_r)\sin(\theta_e-\theta_r) & \frac{3}{2}L_k+\frac{3}{2}L_m\sin^2(\theta_e-\theta_r)+L_{lr} & 0\\ 0 & 0 & L_{lr}\end{bmatrix}$$

(2.95)

From (2.92) - (2.95), the stator and rotor flux equations for a DFIG with dynamic eccentricity in the air gap are

$$\lambda_{qs} = (L_{ls} + \frac{3}{2}L_k + \frac{3}{2}L_m \cos^2(\theta_e - \theta_r))i_{qs} + (\frac{3}{2}L_m \cos(\theta_e - \theta_r)\sin(\theta_e - \theta_r))i_{ds} + (\frac{3}{2}L_k + \frac{3}{2}L_m \cos^2(\theta_e - \theta_r))i_{qr} + (\frac{3}{2}L_m \cos(\theta_e - \theta_r)\sin(\theta_e - \theta_r))i_{dr} \quad (2.96)$$

$$\lambda_{ds} = (\frac{3}{2}L_m \cos(\theta_e - \theta_r)\sin(\theta_e - \theta_r))i_{qs} + (L_{ls} + \frac{3}{2}L_k + \frac{3}{2}L_m \sin^2(\theta_e - \theta_r))i_{ds} + (\frac{3}{2}L_m \cos(\theta_e - \theta_r)\sin(\theta_e - \theta_r))i_{qr} + (\frac{3}{2}L_k + \frac{3}{2}L_m \sin^2(\theta_e - \theta_r))i_{dr} \quad (2.97)$$

$$\lambda_{qr} = (\frac{3}{2}L_k + \frac{3}{2}L_m \cos^2(\theta_e - \theta_r))i_{qs} + (\frac{3}{2}L_m \cos(\theta_e - \theta_r)\sin(\theta_e - \theta_r))i_{ds} + (L_{lr} + \frac{3}{2}L_k + \frac{3}{2}L_m \cos^2(\theta_e - \theta_r))i_{qr} + (\frac{3}{2}L_m \cos(\theta_e - \theta_r)\sin(\theta_e - \theta_r))i_{dr} \quad (2.98)$$

$$\lambda_{dr} = (\frac{3}{2}L_m \cos(\theta_e - \theta_r)\sin(\theta_e - \theta_r))i_{qs} + (\frac{3}{2}L_k + \frac{3}{2}L_m \sin^2(\theta_e - \theta_r))i_{ds} + (\frac{3}{2}L_m \cos(\theta_e - \theta_r)\sin(\theta_e - \theta_r))i_{qr} + (L_{lr} + \frac{3}{2}L_k + \frac{3}{2}L_m \sin^2(\theta_e - \theta_r))i_{dr} \quad (2.99)$$

From (2.96) - (2.99), similar to static air gap eccentricity dynamic eccentricity causes cross coupling in the flux equations and introduces a time varying component of inductance oscillating twice the slip frequency, $2(f_e - f_r)$ ($2\omega_e - 2\omega_r$). This will induce oscillation at the same in the synchronous frame stator and rotor currents, resulting in a torque and stator power oscillations at twice the slip frequency. In the next chapter a different reference frame is introduced to decouple the flux equations under eccentric conditions.

3. DETECTION OF ECCENTRICITY FAULTS IN DFIGS

3.1 Modeling DFIGs with air gap eccentricities

It was shown in the previous chapter that the presence of eccentricity in the air gap causes mutual coupling between the d and q axis fluxes. In the synchronous reference frame a static eccentricity causes a time varying inductance oscillating at *2f*, where f is the synchronous frequency. In a closed-loop controlled DFIG connected to a stiff grid these second harmonic oscillations occur in the stator and hence rotor currents. The higher order harmonics caused by the interaction between the second harmonic current and the time varying inductances can be neglected.

The flux equations in the synchronous frame from (2.83) - (2.86) are shown below

$$\lambda_{qs} = (L_{ls} + \frac{3}{2}L_k + \frac{3}{2}L_m \cos^2\theta_e)i_{qs} + (\frac{3}{2}L_m \cos\theta_e \sin\theta_e)i_{ds} + (\frac{3}{2}L_k + \frac{3}{2}L_m \cos^2\theta_e)i_{qr} + (\frac{3}{2}L_m \cos\theta_e \sin\theta_e)i_{dr}$$

$$\lambda_{ds} = (\frac{3}{2}L_m \cos\theta_e \sin\theta_e)i_{qs} + (L_{ls} + \frac{3}{2}L_k + \frac{3}{2}L_m \sin^2\theta_e)i_{ds} + (\frac{3}{2}L_m \cos\theta_e \sin\theta_e)i_{qr} + (\frac{3}{2}L_k + \frac{3}{2}L_m \sin^2\theta_e)i_{dr}$$

$$\lambda_{qr} = (\frac{3}{2}L_k + \frac{3}{2}L_m \cos^2\theta_e)i_{qs} + (\frac{3}{2}L_m \cos\theta_e \sin\theta_e)i_{ds} + (L_{lr} + \frac{3}{2}L_k + \frac{3}{2}L_m \cos^2\theta_e)i_{qr} + (\frac{3}{2}L_m \cos\theta_e \sin\theta_e)i_{dr}$$

$$\lambda_{dr} = (\frac{3}{2}L_m \cos\theta_e \sin\theta_e)i_{qs} + (\frac{3}{2}L_k + \frac{3}{2}L_m \sin^2\theta_e)i_{ds} + (\frac{3}{2}L_m \cos\theta_e \sin\theta_e)i_{qr} + (L_{lr} + \frac{3}{2}L_k + \frac{3}{2}L_m \sin^2\theta_e)i_{dr}$$

From the above equations it can be seen that the coupling between the d and q axis is due to the double frequency component of the inductance.

It has been shown in [12] that the negative sequence components in the stator current spectrum can be used to detect and estimate the level of static eccentricity. Hence the resulting double frequency component in the d and q axis stator current can be viewed as a current vector moving at an angular speed of $2\omega_e$ in a direction opposite to

the synchronous dq frame. Thus in the stationary abc frame this is a negative sequence current or a current vector rotating at synchronous frequency in a direction opposite to that of the stator current vector. This is illustrated in Fig. 17. Here i_s^f denotes the vector of the current component caused due to the fault.

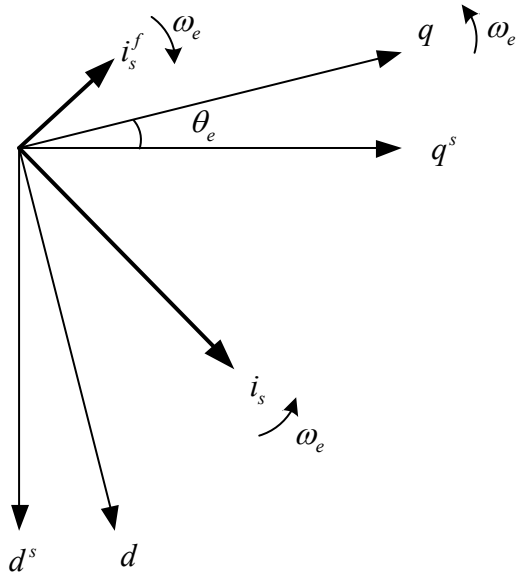

Fig. 17. Vector diagram showing negative sequence stator current component caused by static eccentricity

The flux equations can be decoupled by moving to a reference frame rotating at a speed of ω_e in the clockwise direction with respect to the synchronous reference frame. This is essentially the stationary two axis frame. In this reference frame the stator current moves clockwise at ω_e and the fault current component moves counter clockwise at the same speed.

The voltage equations for the DFIG in the stationary two axis frame can be obtained by setting $\omega_e = 0$ in the healthy machine equations given in (2.28) and (2.29). The notation xy is used to represent this new frame. The voltage equations are given by

$$v_{xys} = p\lambda_{xys} + r_s i_{xys} \tag{3.1}$$

$$v_{xyr} = -\omega_r \begin{bmatrix} 0 & -1 & 0 \\ 1 & 0 & 0 \\ 0 & 0 & 0 \end{bmatrix} \lambda_{xyr} + p\lambda_{xyr} + r_r i_{xyr} \tag{3.2}$$

The flux equations in the xy frame are given by

$$\begin{aligned} \lambda_{xys} &= L_{xys} i_{xys} + L_{xysr} i_{xyr} \\ \lambda_{xyr} &= L_{xyrs} i_{xys} + L_{xyr} i_{xyr} \end{aligned} \tag{3.3}$$

$$L_{xys} = \left[T_{qd}(0)\right] L_{abcs} \left[T_{qd}(0)\right]^{-1} = \begin{bmatrix} L_{ls} + \frac{3}{2}L_k + \frac{3}{2}L_m & 0 & 0 \\ 0 & L_{ls} + \frac{3}{2}L_k & 0 \\ 0 & 0 & 1 \end{bmatrix} \tag{3.4}$$

$$L_{xysr} = \left[T_{qd}(0)\right] L_{abcsr} \left[T_{qd}(-\theta_r)\right]^{-1} = \begin{bmatrix} \frac{3}{2}L_k + \frac{3}{2}L_m & 0 & 0 \\ 0 & \frac{3}{2}L_k & 0 \\ 0 & 0 & 0 \end{bmatrix} \tag{3.5}$$

$$L_{xyrs} = \left[T_{qd}(-\theta_r)\right] L_{abcrs} \left[T_{qd}0)\right]^{-1} = \begin{bmatrix} \frac{3}{2}L_k + \frac{3}{2}L_m & 0 & 0 \\ 0 & \frac{3}{2}L_k & 0 \\ 0 & 0 & 0 \end{bmatrix} \tag{3.6}$$

$$L_{xyr} = \left[T_{qd}(-\theta_r)\right] L_{abcr} \left[T_{qd}(-\theta_r)\right]^{-1} = \begin{bmatrix} L_{ls} + \frac{3}{2}L_k + \frac{3}{2}L_m & 0 & 0 \\ 0 & L_{ls} + \frac{3}{2}L_k & 0 \\ 0 & 0 & 1 \end{bmatrix} \quad (3.7)$$

Hence in the stationary two axis reference frame the flux equations of the DFIG with static eccentricity are decoupled.

In the case of a dynamic eccentricity the flux equations in the synchronous reference frame from (2.96) - (2.99). Extending the explanation for static eccentricity, under stiff grid voltage conditions a closed-loop controlled DFIG with dynamic eccentricity in the air gap will have frequency components at $2f$ - $2f_r$ in the synchronous frame stator and rotor currents, caused by the time varying inductances. This fault current component can be viewed as a current vector rotating at a speed of $2\omega_e$ - $2\omega_r$ in the clockwise direction with respect to the synchronous dq frame. In the stationary abc frame this is a frequency component at $2f_r$ - f_e. This is illustrated in the Fig. 18.

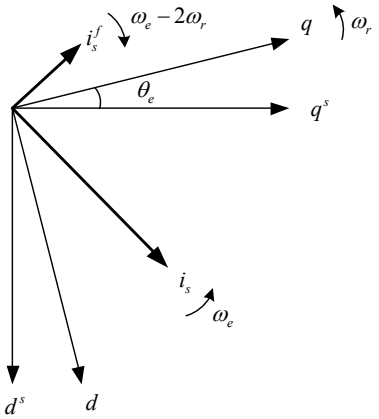

Fig. 18. Vector diagram showing the fault current component caused by dynamic eccentricity

Similar to the static eccentricity case, the flux equations can be decoupled by moving to a frame rotating at ω_r in the counterclockwise direction. In such a frame the stator fault current component rotates at ω_e - ω_r in the clockwise direction and the stator current rotates at the same speed in the counterclockwise direction.

The voltage and flux equations can be obtained similar to the static eccentricity case and are as follows

$$v_{xys} = \omega_r \begin{bmatrix} 0 & 1 & 0 \\ -1 & 0 & 0 \\ 0 & 0 & 0 \end{bmatrix} \lambda_{xys} + p\lambda_{xys} + r_s i_{xys} \tag{3.8}$$

$$v_{xyr} = p\lambda_{xyr} + r_r i_{xyr} \tag{3.9}$$

$$\begin{aligned} \lambda_{xys} &= L_{xys} i_{xys} + L_{xysr} i_{xyr} \\ \lambda_{xyr} &= L_{xyrs} i_{xys} + L_{xyr} i_{xyr} \end{aligned} \tag{3.10}$$

$$L_{xys} = \left[T_{qd}(\theta_r)\right] L_{abcs} \left[T_{qd}(\theta_r)\right]^{-1} = \begin{bmatrix} L_{ls} + \frac{3}{2}L_k + \frac{3}{2}L_m & 0 & 0 \\ 0 & L_{ls} + \frac{3}{2}L_k & 0 \\ 0 & 0 & 1 \end{bmatrix} \tag{3.11}$$

$$L_{xysr} = \left[T_{qd}(\theta_r)\right] L_{abcsr} \left[T_{qd}(0)\right]^{-1} = \begin{bmatrix} \frac{3}{2}L_k + \frac{3}{2}L_m & 0 & 0 \\ 0 & \frac{3}{2}L_k & 0 \\ 0 & 0 & 0 \end{bmatrix} \tag{3.12}$$

$$L_{xyrs} = \left[T_{qd}(0)\right] L_{abcrs} \left[T_{qd}(\theta_r)\right]^{-1} = \begin{bmatrix} \frac{3}{2}L_k + \frac{3}{2}L_m & 0 & 0 \\ 0 & \frac{3}{2}L_k & 0 \\ 0 & 0 & 0 \end{bmatrix} \tag{3.13}$$

$$L_{xyr} = \left[T_{qd}(0)\right] L_{abcr} \left[T_{qd}(0)\right]^{-1} = \begin{bmatrix} L_{ls} + \frac{3}{2}L_k + \frac{3}{2}L_m & 0 & 0 \\ 0 & L_{ls} + \frac{3}{2}L_k & 0 \\ 0 & 0 & 1 \end{bmatrix} \tag{3.14}$$

Using equations (3.1) - (3.14), models of the DFIG can be built in MATLAB® Simulink®. The basic block diagram of the model is shown in the Fig. 19.

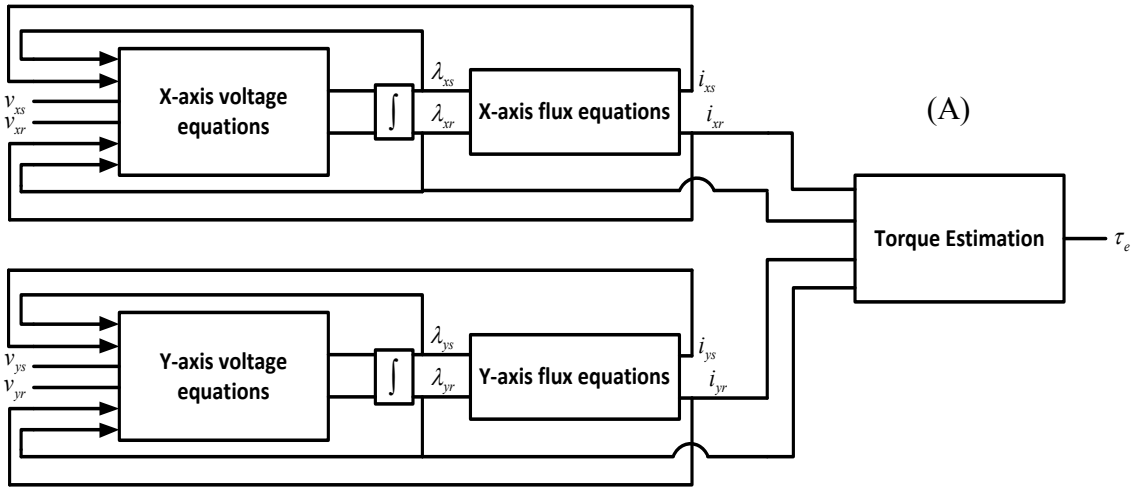

Fig. 19. (A) DFIG with static air gap eccentricity. (B) DFIG with dynamic air gap eccentricity

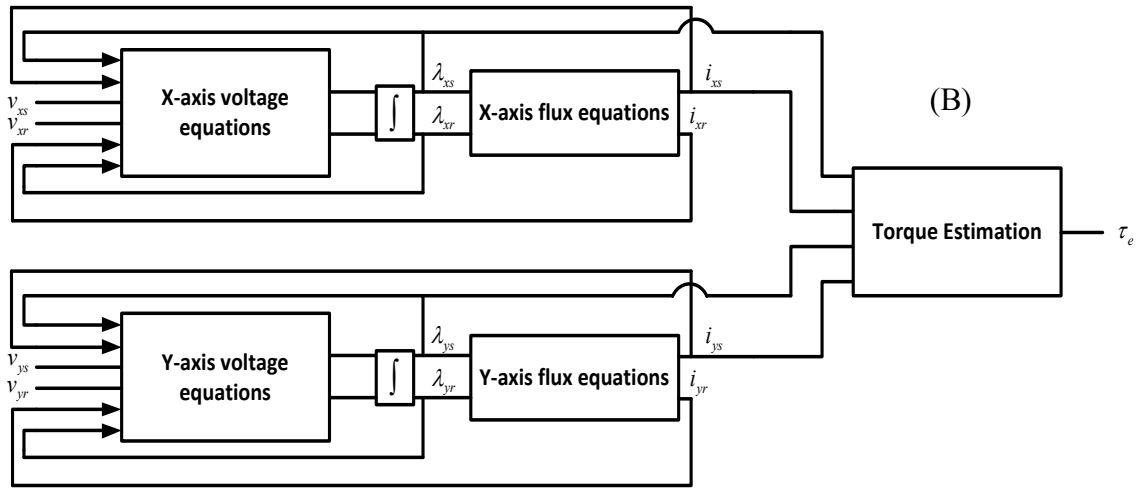

Fig. 19. continued

3.2 Effect of closed-loop on fault signatures

In the previous section it was identified that due to air gap eccentricity, new frequency components appear in the synchronous frame stator current spectrum. Since the voltage is fixed by the grid it is has a constant value in the synchronous frame. As a result if the DFIG is controlled using stator flux orientation, from (2.38), the frequency components will appear in the stator real and reactive power spectrum. The primary frequency components in the power caused by the fault are the clockwise rotating $2\omega_e$ component for static air gap eccentricities and clockwise rotating $2\omega_e$ - $2\omega_r$ component for dynamic air gap eccentricities.

For a DFIG operated for closed-loop stator power control using the scheme discussed in the second chapter the inner and outer control loops are shown in Fig. 20.

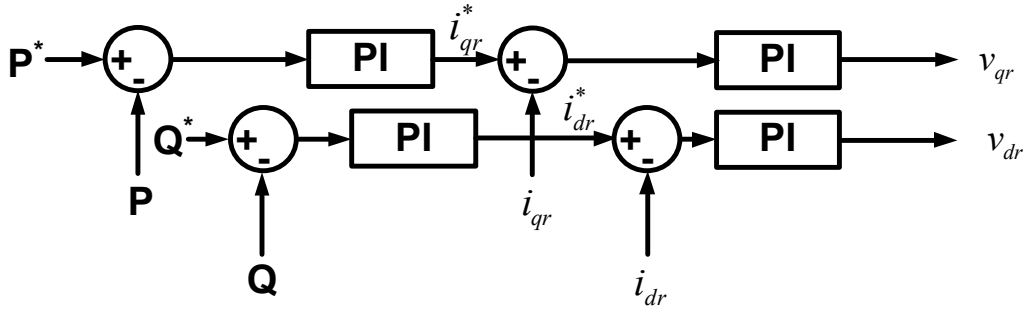

Fig. 20. Inner and outer control loops of rotor side converter of a DFIG

As explained earlier in the presence of static eccentricity $2\omega_e$ component appears in the real and reactive power. For a constant power command the compensation provide by the PI controllers in the outer control loop for this component depends on the closed-loop bandwidth. So the extents of attenuation the double frequency ripple in d and q axis current and hence stator real and reactive power depends on the controller gains.

From the flux equations in the synchronous reference frame in (2.83) - (2.86), there is a constant and oscillating component of each inductance. The oscillating component is responsible for the ripple in the synchronous frame current and the power. Separating the constant inductance from the oscillating component the equations reduce to

$$\begin{aligned}
\lambda_{qs1} &= (L_{ls} + \frac{3}{2}L_k + \frac{3}{4}L_m)i_{qs1} + (\frac{3}{2}L_k + \frac{3}{4}L_m)i_{qr1} \\
\lambda_{ds1} &= (L_{ls} + \frac{3}{2}L_k + \frac{3}{4}L_m)i_{ds1} + (\frac{3}{2}L_k + \frac{3}{4}L_m)i_{dr1} \\
\lambda_{qr1} &= (\frac{3}{2}L_k + \frac{3}{4}L_m)i_{qs1} + (L_{lr} + \frac{3}{2}L_k + \frac{3}{4}L_m)i_{qr1} \\
\lambda_{dr1} &= (\frac{3}{2}L_k + \frac{3}{4}L_m)i_{ds1} + (L_{lr} + \frac{3}{2}L_k + \frac{3}{4}L_m)i_{dr1}
\end{aligned} \tag{3.15}$$

In (3.15) the subscript '1' refers to the constant part of the flux and current in the synchronous reference frame. The constant current components caused by the interaction of the higher frequency current component with the oscillating component of the inductance are neglected. This assumption is valid for eccentricities up to 80%. If there is no eccentricity in the air gap the above equations can be reduced to

$$\begin{aligned}
\lambda_{qs} &= (L_{ls} + \frac{3}{2}L_k)i_{qs} + (\frac{3}{2}L_k)i_{qr} \\
\lambda_{ds} &= (L_{ls} + \frac{3}{2}L_k)i_{ds} + (\frac{3}{2}L_k)i_{dr} \\
\lambda_{qr} &= (\frac{3}{2}L_k)i_{qs} + (L_{lr} + \frac{3}{2}L_k)i_{qr} \\
\lambda_{dr} &= (\frac{3}{2}L_k)i_{ds} + (L_{lr} + \frac{3}{2}L_k)i_{dr}
\end{aligned} \tag{3.16}$$

In (3.16) there is no oscillating component in the inductance, current or flux and the subscript '1' is removed. From (3.15) and (3.16) it can be concluded that is an increase in the constant inductance when a static eccentricity is introduced in the air gap.

When the DFIG is controlled in a closed-loop with the stator flux oriented along the d axis, the equation for estimation of rotor current command from the stator power command is given by

$$\begin{aligned}
i_{qr} &= -\frac{2}{3}\frac{P}{V_m}\frac{\left(L_{ls} + \frac{3}{2}L_k\right)}{\left(\frac{3}{2}L_k\right)} \\
i_{dr} &= \frac{\lambda_{ds}}{\left(\frac{3}{2}L_k\right)} - \frac{2}{3}\frac{Q}{V_m}\frac{\left(L_{ls} + \frac{3}{2}L_k\right)}{\left(\frac{3}{2}L_k\right)}
\end{aligned} \tag{3.17}$$

Equation (3.17) is obtained by substituting for the inductance from (3.16) in (2.42) and (2.43). In the presence of eccentricity L_k increases from(2.75), and an additional term $0.75L_m$ is added to the inductances which increases the net inductance. The effect of this addition is negligible in the q axis rotor current equation since it occurs in the numerator and denominator, but there is a significant change in the d axis rotor current due to the stator flux term.

Since the controller is designed using the healthy machine parameters, the estimated d axis rotor current is much higher than that required to supply the commanded reactive power. In a practical system the outer loop is closed using a PI controller. The design of the gains of this controller was discussed in the previous chapter.

Due to the integral action of the controller, the error in the estimated d axis rotor current caused by the effect of increase in the constant component of the inductance is compensated. As a result, for a DFIG operated for closed-loop stator power control, the only effect of static eccentricity in the air gap is the $2f$ component in the real and reactive power. The magnitude of this component is also dependent on the controller gains and hence the bandwidths of the closed-loop system.

In the case of dynamic eccentricity the flux equations in the synchronous reference frame are given by (2.96) - (2.99). It can be observed that here the oscillating component of the inductance has a frequency of $2f - 2f_r$ and will cause a ripple of the same frequency in the synchronous frame stator current and stator real and reactive power. So in the case of dynamic eccentricity the compensation of the $2f - 2f_r$ ripple in

the real and reactive power by the PI controllers in the outer loops depends on the gain of the closed-loop at the specific disturbance frequency. The disturbance frequency changes with rotor speed and hence the compensation will differ at different rotor speeds. When the rotor speed comes close to the synchronous speed the disturbance frequency is close to zero and the compensation is high due to the integral action of the PI controller. Separating the constant inductance terms from the time varying components gives equations identical to (3.15). Similar to the case of static eccentricity from (3.17), in the presence of eccentricity L_k increases from (2.75), and an additional term $0.75L_m$ is added to the inductances which increases the net inductance. The estimated d axis rotor current is thus much higher than that required to supply the commanded reactive power.

Due to the integral action of the PI controller in the outer power loop the error in the rotor current command is compensated and the only available signature is the $2f - 2f_r$ component in the real and reactive power. Effective detection thus depends on the controller gains and the speed of rotation of the rotor, since this affects the signature frequency.

3.3 Isolating eccentricity faults

An unbalanced voltage or current can be expressed as a sum of positive and negative sequence components. Hence an unbalance in the grid voltage caused by a fault in the line, will cause negative sequence components in the voltages and hence stator current. This will appear as a $2f$ component in the frequency spectrum of the synchronous frame current and real and reactive stator power. So the signatures in the

power spectrum caused by unbalanced grid voltages will interfere with those caused by static air gap eccentricity. In a closed-loop controlled DFIG it is difficult to isolate the cause of a *2f* component in the power spectrum since multiple faults produce identical signatures. However it is clear that an unbalance in the stator does not affect the constant component of the inductance unlike a static eccentricity, and hence there is not error in the estimation of the d and q axis rotor current. A similar explanation can be extended for $2f - 2f_r$ component that is caused by dynamic air gap eccentricities. The expression for the electrical torque in terms of stator fluxes an currents is given by

$$\tau_e = \frac{3}{2}\frac{P}{2}\left(\lambda_{ds} i_{qs} - \lambda_{qs} i_{ds}\right) \tag{3.18}$$

For a DFIG operating in closed-loop and connected to a stiff grid, the stator flux is a constant and oriented along the d axis, $\lambda_{qs}=0$. From(3.18), any oscillation in the load torque, will be reflected in the electrical torque and hence the q axis stator current. So load torque oscillations at twice the slip frequency will cause $2f - 2f_r$ component in the synchronous frame stator current and the stator real power.

An unbalance in the rotor windings caused by inter-turn faults will cause negative sequence components in the rotor circuit. Since the frequency of the rotor current is at *sf*, the negative sequence frequency components will be at *–sf*. Here *s* represents the slip of the rotor. This *–sf* component on the rotor is reflected on the stator current at *(1-2s)f*. This corresponds to a frequency of $2f_r - f_e$ in the stator current spectrum and a $2f - 2f_r$ component rotating in the clockwise direction in the synchronous frame stator current. In a DFIG the $2f - 2f_r$ component occurs in the stator real and reactive power. Hence, an electrical unbalance in the rotor and load torque oscillations at slip

frequency can cause the same signatures produced by a dynamic eccentricity in the air gap. But similar to the static eccentricity case, neither of these faults affects the inductance values.

A general conclusion from the above discussion is that the change in the magnitude of the inductance can be used as a definite way to distinguish eccentricity faults from electrical asymmetries that cause identical effects on the current and hence stator power spectrum.

The compensation of the error in the rotor command caused by the change in the magnitude of the constant component of the inductance is due to the integral action of the PI controller in the outer control loop. If this compensation is not provided the generated reactive power supplied to stator will be higher than the commanded value as seen from (3.17).

The control loop can thus be modified to make eccentricity faults identifiable. This however requires knowledge of the d axis stator flux in the synchronous reference frame. The stator flux can be estimated using the stator voltages in the synchronous frame according to the following equations.

$$\lambda_{ds}^{s} = \int \left(v_{ds}^{s} - i_{ds}^{s} r_{s} \right) . dt \tag{3.19}$$

$$\lambda_{qs}^{s} = \int \left(v_{qs}^{s} - i_{qs}^{s} r_{s} \right) . dt \tag{3.20}$$

The flux is then transformed to the synchronous frame using the stator angle which is estimated from the stator stationary frame voltages using (2.35). In a practical DFIG system the stator voltages and currents are sensed. A block diagram for stator flux estimation is shown in Fig. 21.

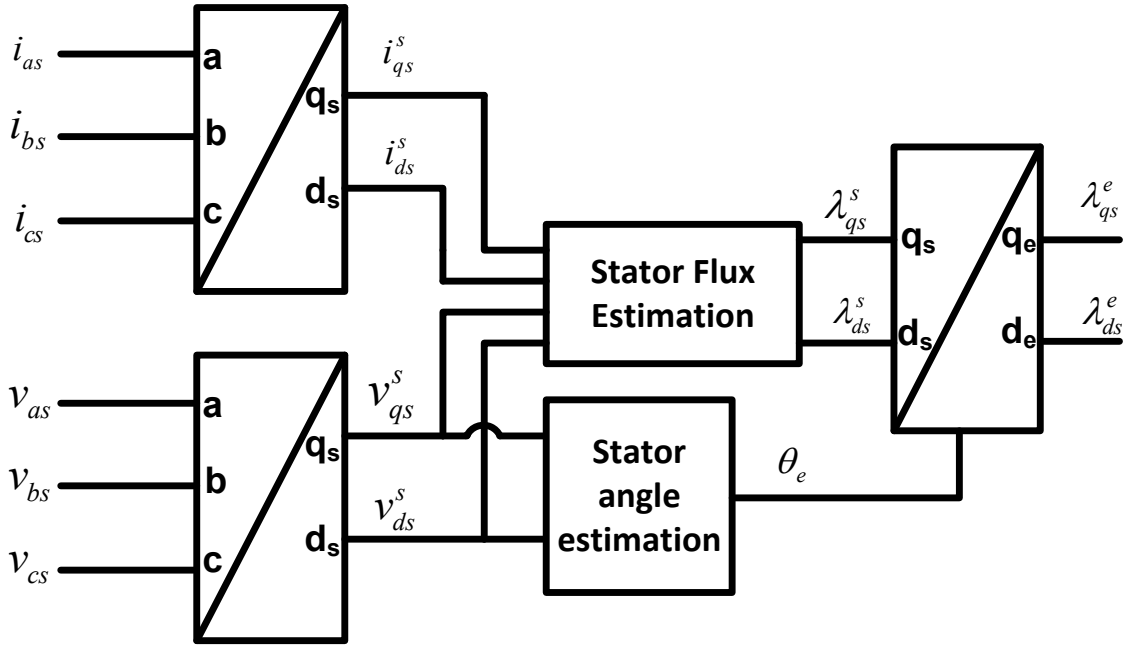

Fig. 21. Stator flux estimation

Since the stator voltage is oriented along the q axis, for a negligible resistive drop on the stator, the q axis flux is zero. Since the flux is known the machine inductances can be used to close the loop as shown in Fig. 22.

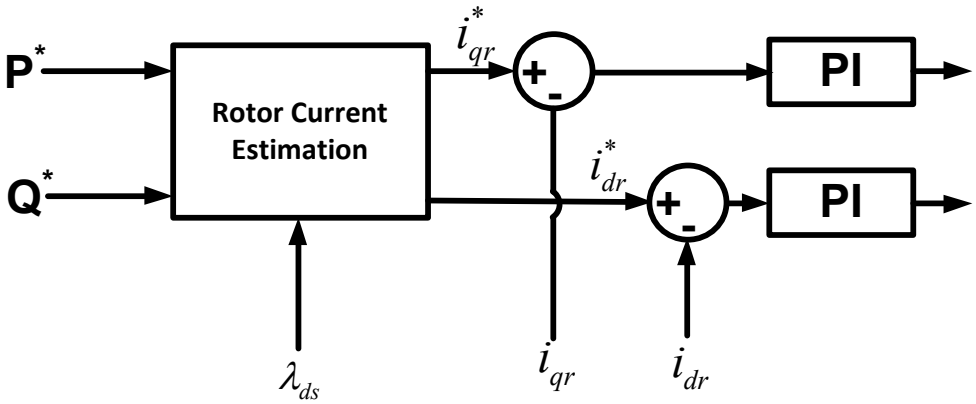

Fig. 22. Modified outer control loop for eccentricity detection

By using the healthy machine parameters for rotor current estimation, eccentricity faults can be detected by tracking the supplied reactive power.

Under static air gap eccentricities the reactive power has a *2f* component in the frequency spectrum and the supplied reactive power does not track the commanded value. The extent of deviation from the command is proportional to the level of static eccentricity.

Under dynamic air gap eccentricities the reactive power has a $2f - 2f_r$ component in the frequency spectrum and the supplied reactive power does not track the commanded value. The extent of deviation from the command is proportional to the level of dynamic eccentricity.

Similar frequency components caused by other faults like, stator and rotor unbalance and load torque oscillations; will not cause the error in the reactive power output.

The major drawback with using the proposed control is that it requires accurate knowledge of the machine inductances, particularly the magnetizing inductance L_m. The DFIG is operated for closed-loop power control over a limited range of around 30% of its rated output. The variation of magnetizing inductance due to saturation can be determined over this operating range and a look-up table can be used for estimating the rotor currents from the power command. The proposed method can thus be used to effectively isolate and detect air gap eccentricities in DFIGs operated for closed-loop power control.

4. SIMULATION AND EXPERIMENTAL VALIDATION

4.1 Simulation results

Using the block diagram of the eccentric machine from Fig. 19 a model of the machine is built in MATLAB® Simulink®. A 1hp 4-pole, DFIG with parameters shown in Table I is used.

TABLE I
SPECIFICATIONS OF 1HP DFIG

PARAMETER	***VALUE***
Stator resistance per phase (r_s)	3.35Ω
Stator leakage inductance per phase (L_{ls})	6.94 mH
Magnetizing inductance (L_m)	163.73 mH
Rotor resistance per phase (L'_{lr})	6.94 mH
Stator leakage inductance per phase (r'_r)	1.99 Ω

The relative eccentricity E is made a variable input in the model and initialized before running the simulation. An input of E = 0 represents a healthy machine with no eccentricity in the air gap. The DFIG model with static air gap eccentricity is built in the stationary frame and the model with dynamic eccentricity is built in the rotor reference frame to decouple the flux equations. Stator angle is estimated using the stator voltages according to (2.35) and the gains of the PI controllers are determined according to (2.50) and (2.51).

If the grid voltage is not stiff, negative sequence components in the current will cause identical components in the stator voltage of the DFIG. In order to incorporate this effect in the simulation model a balanced three phase resistive load is connected in

parallel to the stator of the DFIG. Both the DFIG and the resistive load are fed through a 1km long π-model transmission line from the grid. The grid frequency is fixed at 60Hz. The rotor is fed through an inverter block with a constant DC bus voltage. The inverter block uses switching functions to modulate the reference using sinusoidal pulse width modulation (SPWM) at a switching frequency of 20 kHz. The output of the inverter is connected directly to the rotor circuit. The rotor of the DFIG is rotated at a constant speed of 0.7p.u. A layout of the simulation model is shown in Fig. 23.

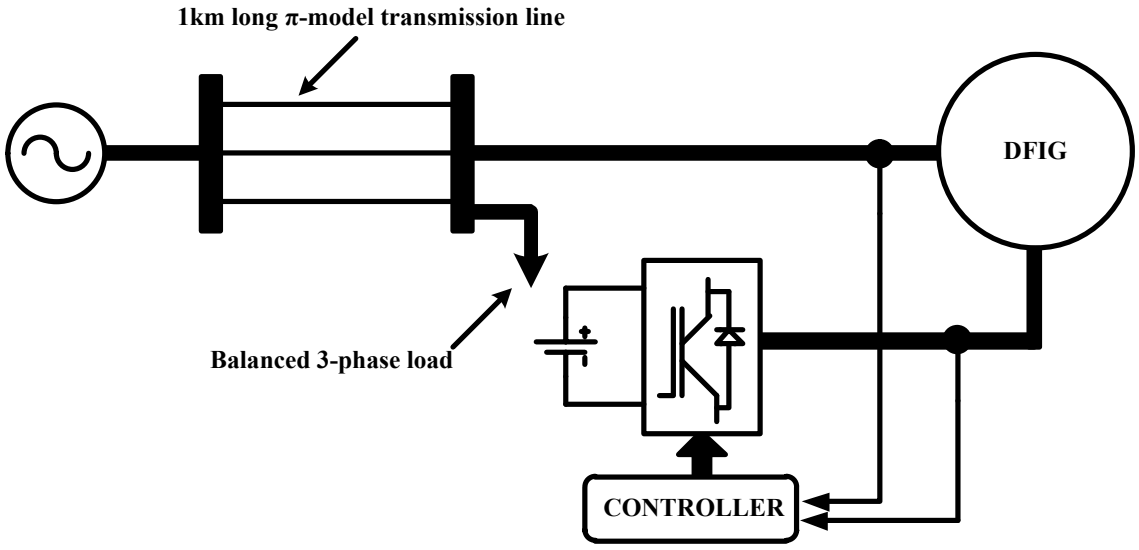

Fig. 23. Layout of simulation model of DFIG

Various cases are studied to verify the proposed modification in the control method. The results obtained are presented in the following section. All the FFT waveforms are plotted on a log scale taking 20 kHz as the fundamental frequency. The magnitude of each frequency component is expressed as a percentage of the value of the 20 kHz component.

4.1.1 Case I

The DFIG is run at a constant speed and controlled using the conventional control scheme with two PI loops. The real power command is initially fixed at 400W and the reactive power at 100W. A step function is used to change the real power command to 500W and reactive power command to 0W at a simulation time of 0.6s. The results obtained for a healthy DFIG shown in Fig. 24, are compared with those obtained for a DFIG with 50% static and 50% dynamic eccentricity in the air gap when using the conventional control. It can be seen from Fig. 25 that using the conventional control scheme, a static eccentricity in the air gap causes second harmonic ripple (*2f*) in the reactive power. Due to integral action in the outer PI loop the errors caused by change in inductance under eccentricity are compensated and the average reactive power is found to track the command value. In Fig. 26 the rotor is driven at an electrical speed of 0.6p.u. As expected in the presence of dynamic eccentricity a frequency component at $2f - 2f_r$ is appears in the stator reactive power. This corresponds to a frequency of 48 Hz. In the case of dynamic eccentricity the fault frequency or signature frequency is a function of rotor speed. As a result the extent of compensation provided by the control system is dependent on the closed-loop gain at the disturbance frequency. This has been illustrated in Fig. 27, where the rotor electrical speed is increased to 0.85p.u. This decreases the fault frequency to 18 Hz. It can be seen that the magnitude of the signature has decreased compared to the Fig. 26. Sensing frequency components that are too close to the DC value is also difficult, since this requires larger sampling windows.

A)

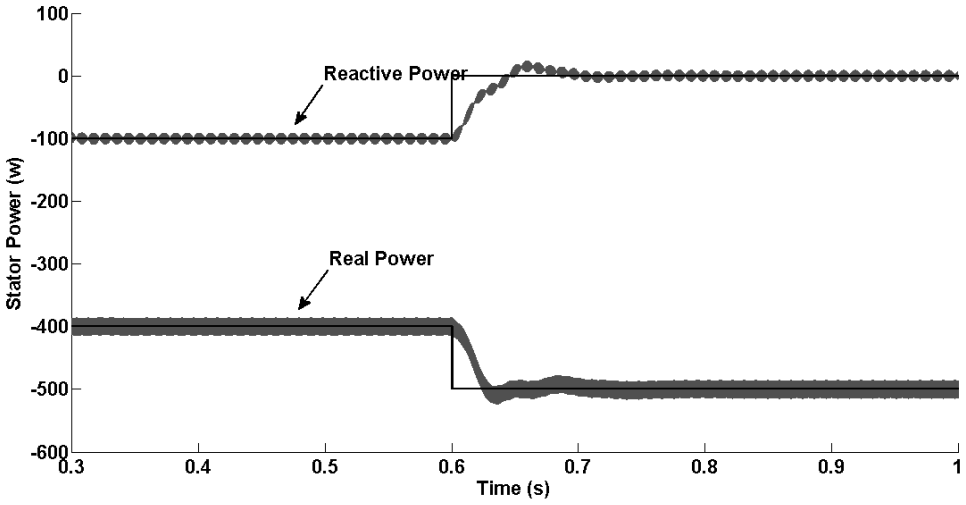

B)

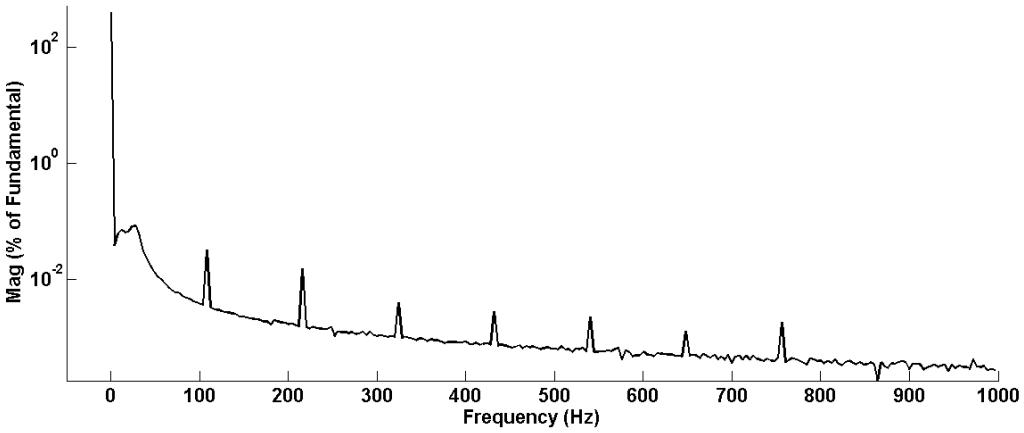

Fig. 24. Conventional control scheme applied to a healthy DFIG A) Stator power command and output B) FFT of the stator reactive power

A)

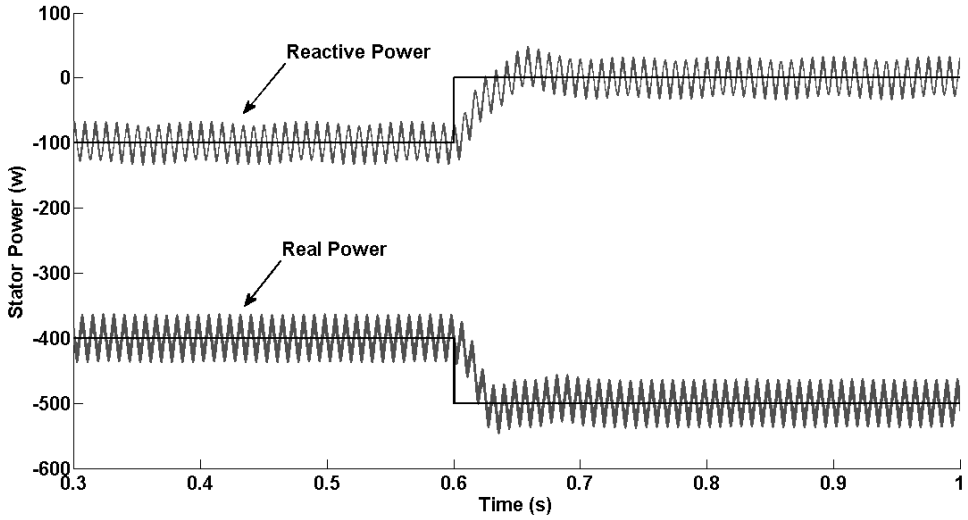

B)

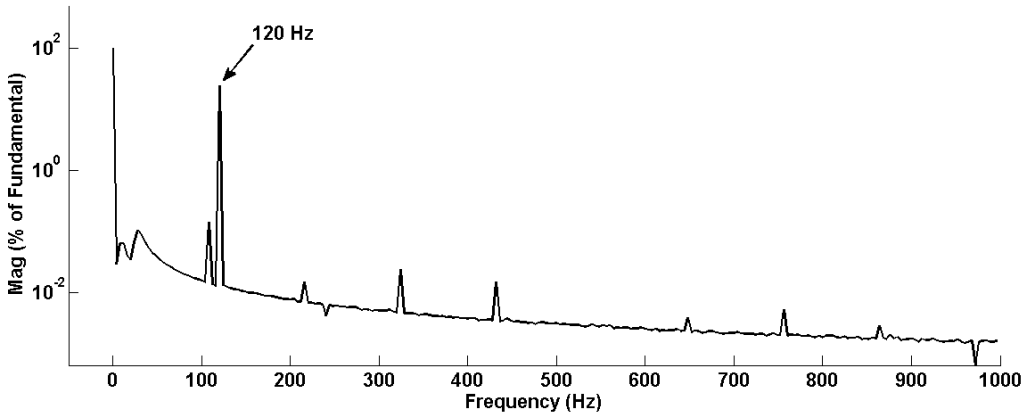

Fig. 25. Conventional control scheme applied to a DFIG with 50% static air gap eccentricity A) Stator power command and output B) FFT of stator reactive power with a 120 Hz (*2f*) fault signature

A)

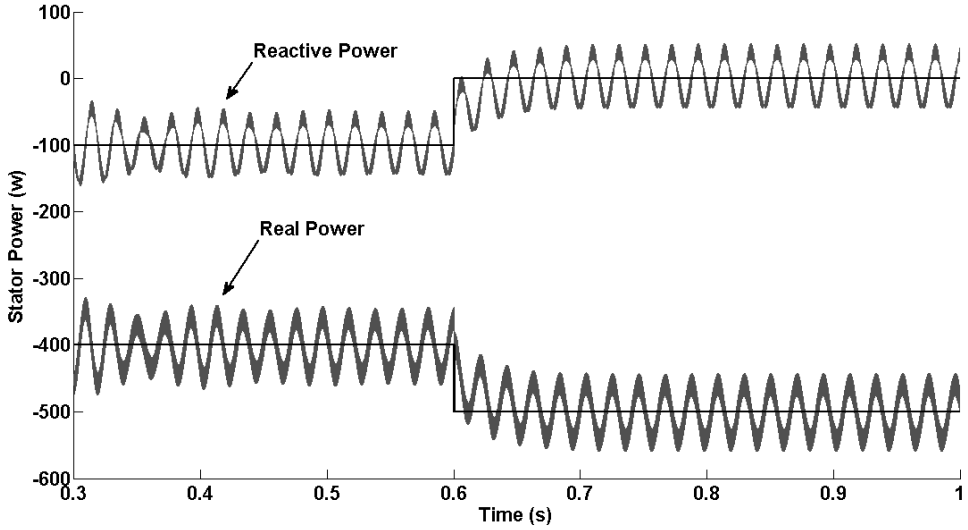

B)

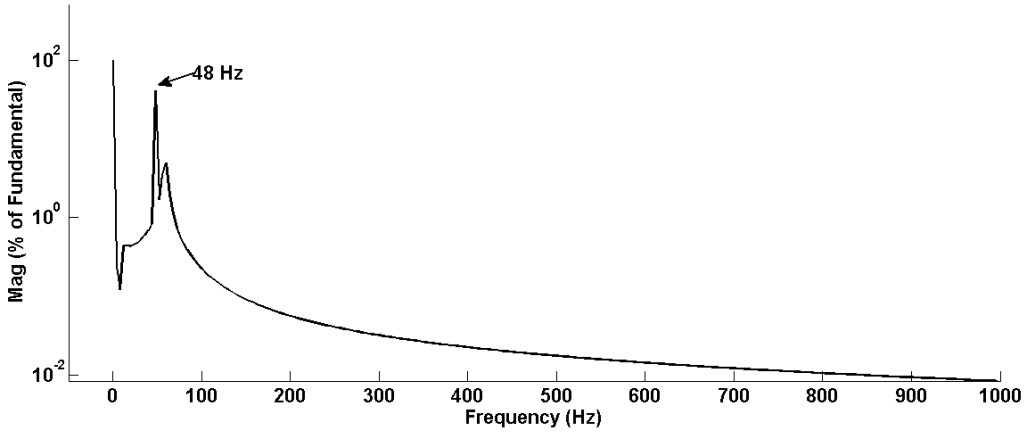

Fig. 26. DFIG with 50% dynamic eccentricity running at an electrical speed of 0.6p.u A) Stator power command and output B) FFT of stator reactive power with fault signature at 48 HZ corresponding to $2f\text{-}2f_r$ frequency component

A)

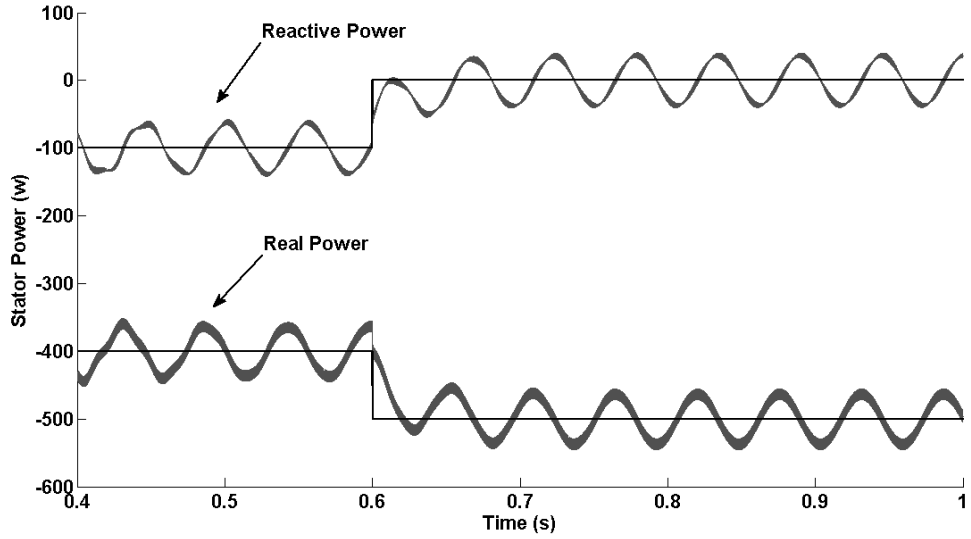

B)

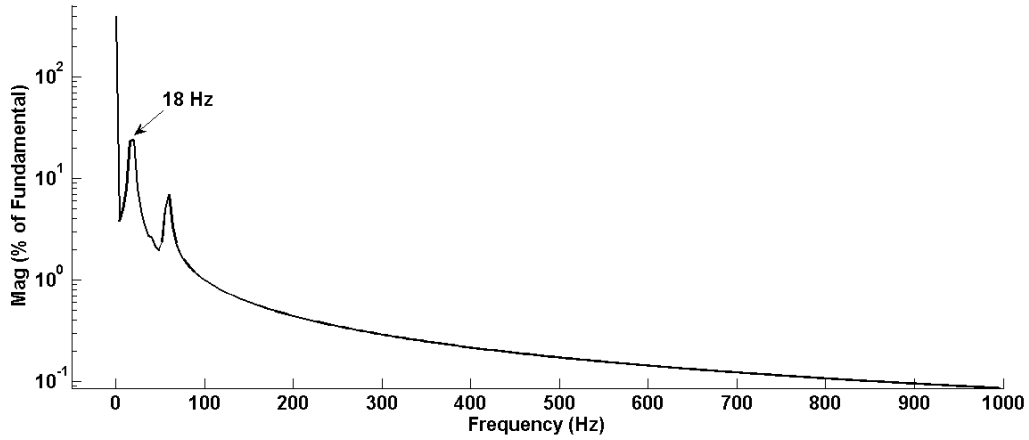

Fig. 27. DFIG with 50% dynamic eccentricity running at an electrical speed of 0.85p.u A) Stator power command and output B) Reactive power spectrum with fault signature at 18Hz

4.1.2 Case II

The effectiveness of the proposed control is verified. The DFIG is run at a constant speed of 0.7p.u in closed-loop. Similar to Case I, a step variation is introduced in the command real and reactive power. The results obtained from the modified control are compared to the conventional control scheme for a healthy machine shown in Fig. 28 and a DFIG with 50% static and dynamic eccentricity in the air gap. The eccentricity is then increased to 60% to study the effect on the delivered reactive power. From Fig. 29, under 50% static eccentricity the reactive power delivered to the stator does not follow the command value, since there is not compensation provided by the control system for the error in the estimated rotor current command caused by increased inductances of the eccentric machine. For a 50% eccentricity the error is 50w. The results obtained for dynamic air gap eccentricity show similar effects as seen from Fig. 30. When the eccentricity is increased to 65% (Fig. 31), the error increases to 70w. This can be used as an index to estimate the amount of eccentricity in the air gap. The signature frequencies caused by the eccentricity in the previous case are also present in the reactive power. When the modified control is applied to a healthy machine the stator power is found to effectively follow the command.

The extent of deviation of the reactive power from the command can thus be used to estimate the amount of eccentricity in the air gap. These two effects can be used to isolate eccentricity faults from other electrical faults in closed-loop controlled DFIGs. The proposed control method can be used as a diagnostic tool to detect eccentricity faults.

A)

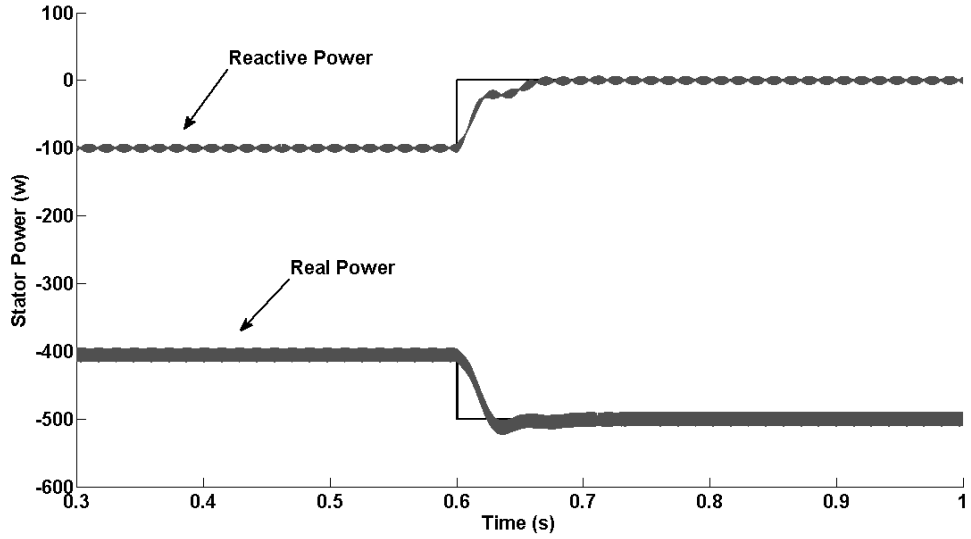

B)

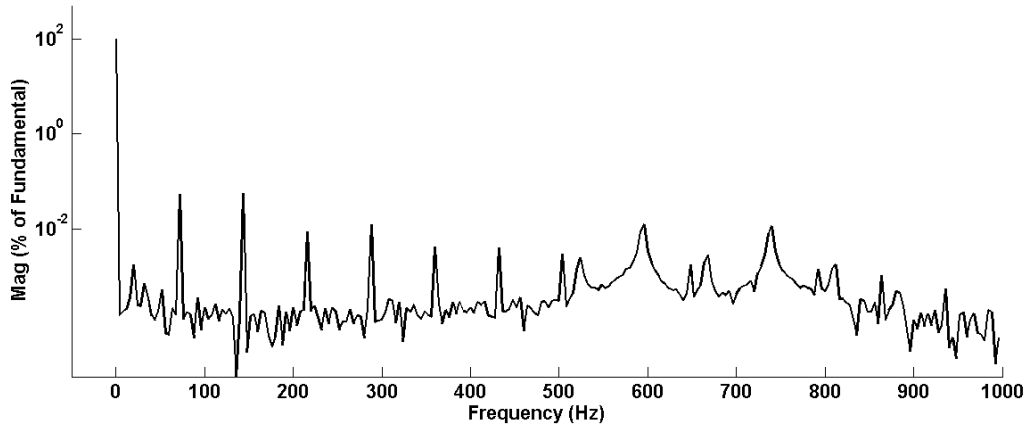

Fig. 28. Modified control applied to a healthy DFIG A) Stator power command and output B) Frequency spectrum of stator reactive power

A)

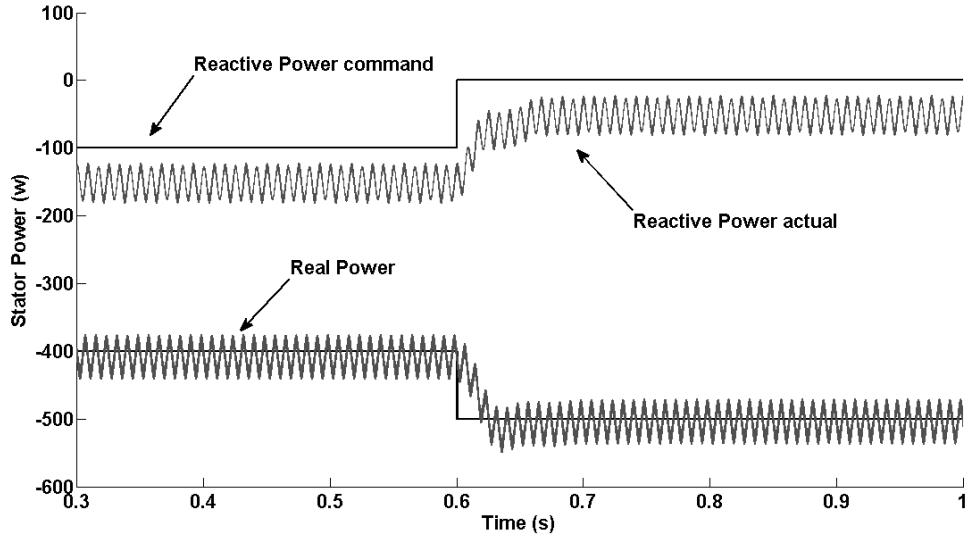

B)

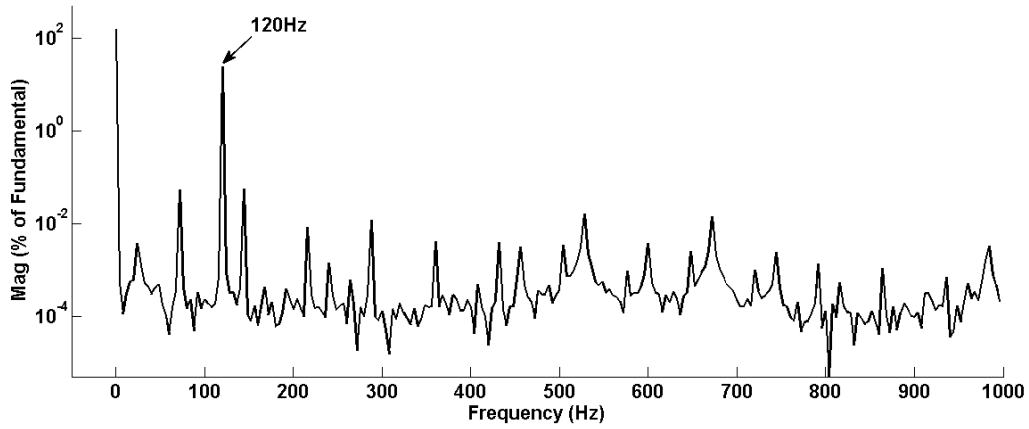

Fig. 29. DFIG with 50% static eccentricity controlled using the modified control method A) Stator power command and output. The reactive power output does not follow the command B) Frequency spectrum of reactive power with fault signatures

A)

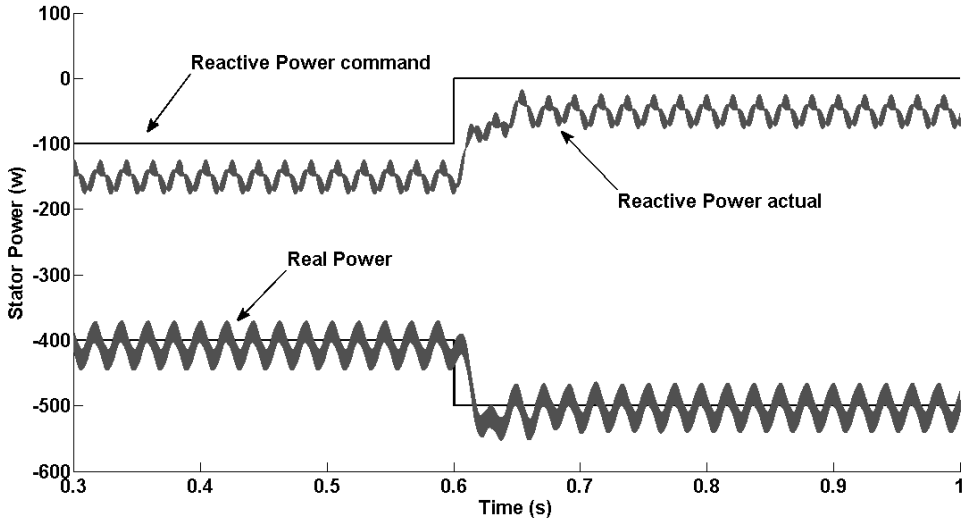

B)

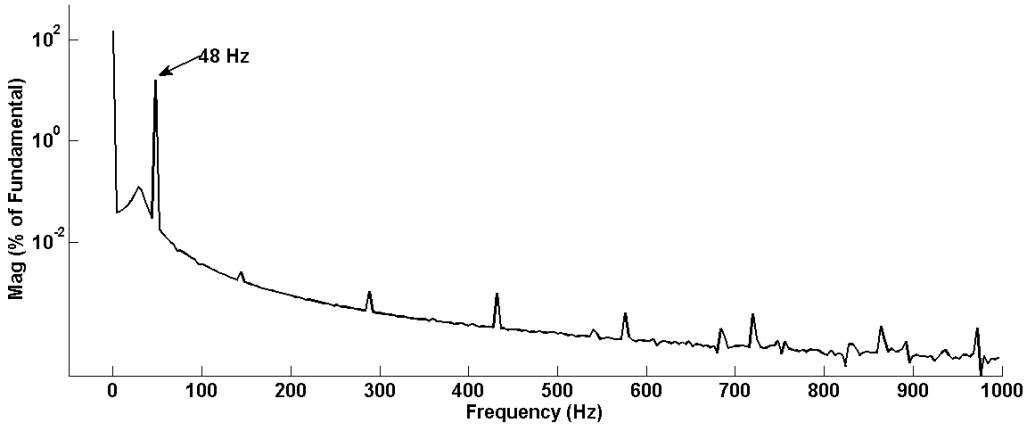

Fig. 30. DFIG with 50% dynamic eccentricity in the air gap running at an electrical speed of 0.6p.u A) Stator power command and output. Reactive power does not follow command B) FFT of reactive power with fault signatures

A)

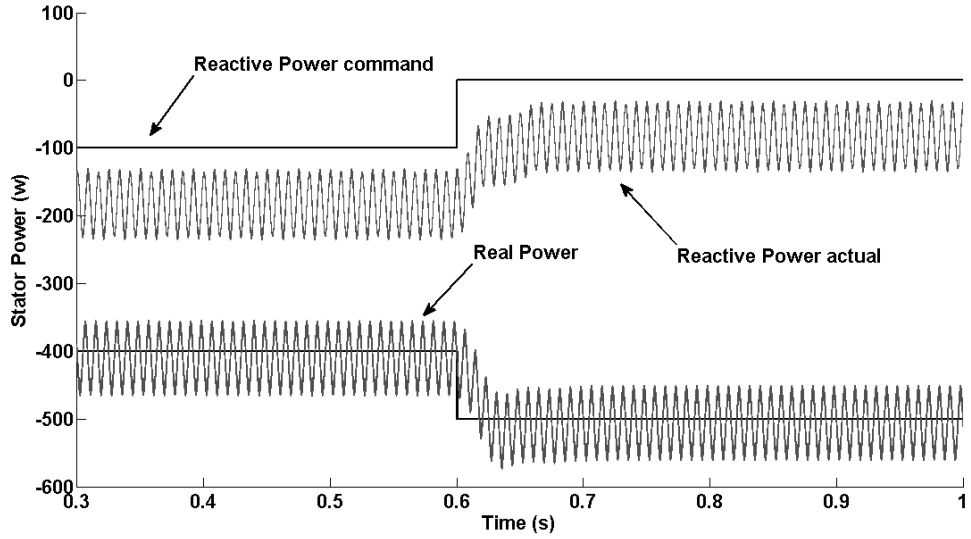

B)

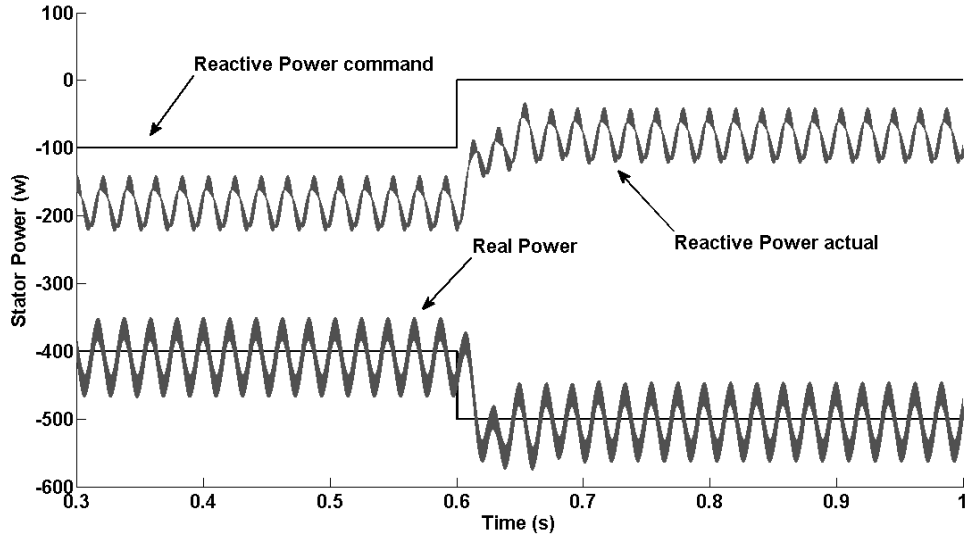

Fig. 31. DFIG with 65% dynamic eccentricity in the air gap A) Stator power output for static eccentricity B) Stator power output for dynamic eccentricity. The error in the delivered reactive power is found to increase with eccentricty.

4.1.3 Case III

It has been explained in the previous chapter electrical unbalances in the stator causes a *2f* component in the real and reactive power output similar to the case of static eccentricity. This is simulated by changing one of the phase resistances of the three phase load connected in parallel to the stator of the DFIG, shown in Fig. 23. As seen from Fig. 32 and Fig. 33, both control methods cause a second harmonic ripple in the reactive power. Thus when using the conventional control, static air gap eccentricities cause the same effect as an unbalance in the stator circuit and it is difficult to isolate the source of the fault. The modified control technique can separate the two causes using the error in the reactive power output which is caused only for eccentric faults. In the case of dynamic eccentricities, torque oscillation and electrical unbalance in the rotor circuit also produce similar signatures.

A)

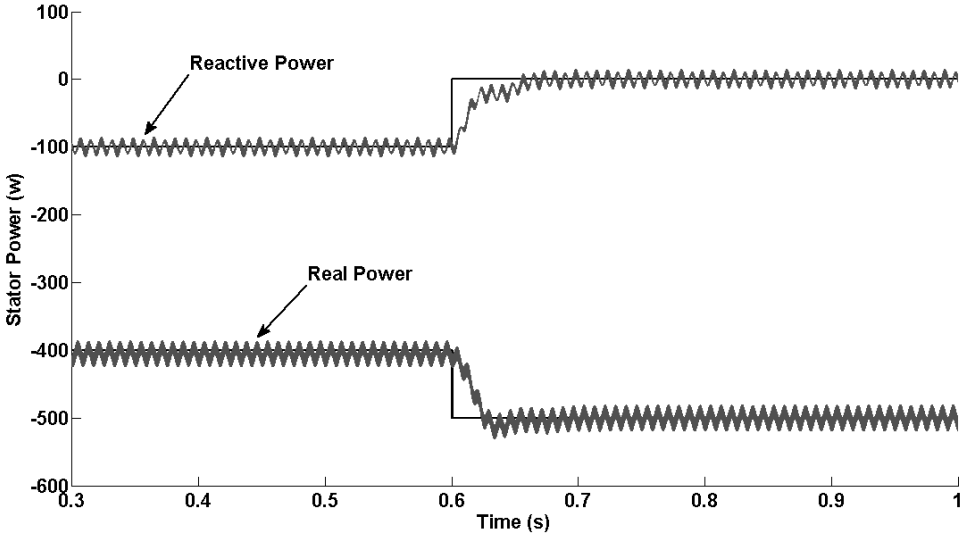

B)

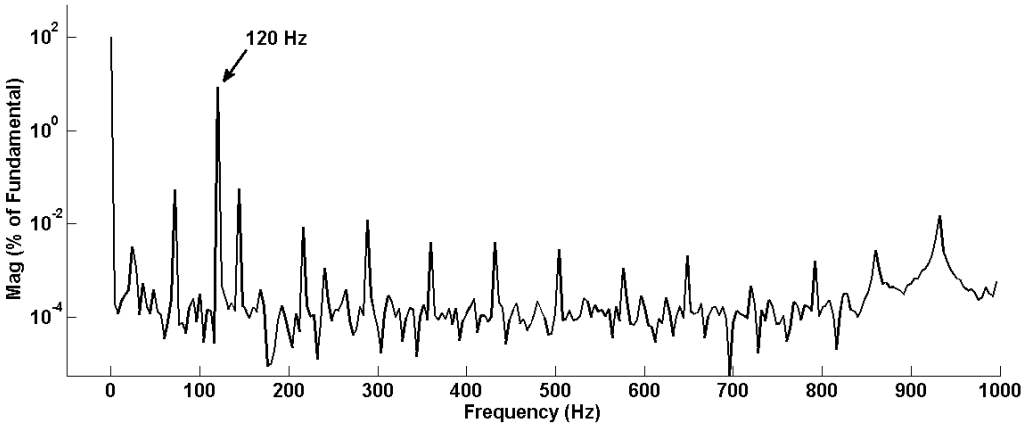

Fig. 32. DFIG with electrical unbalance in the stator A) Stator power output using modified control scheme B) FFT of reactive power

A)

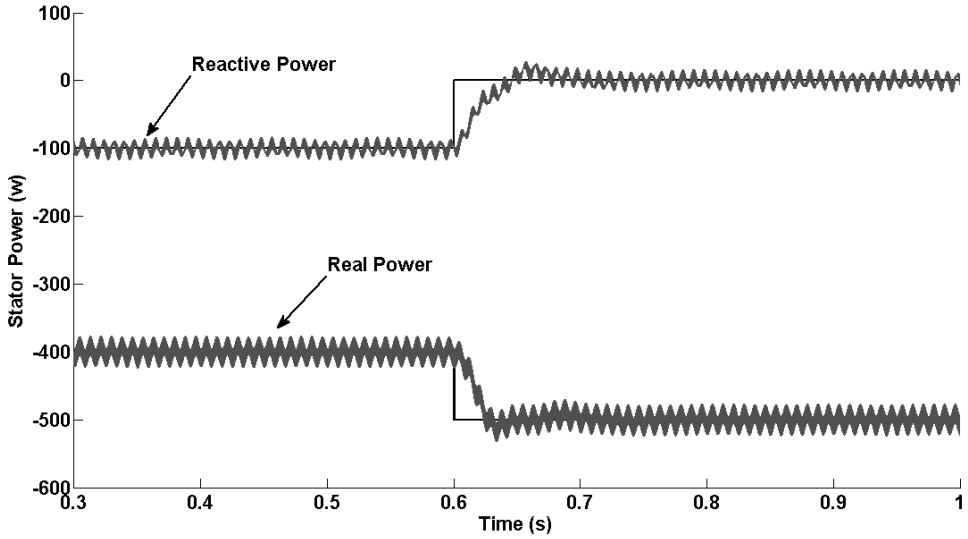

B)

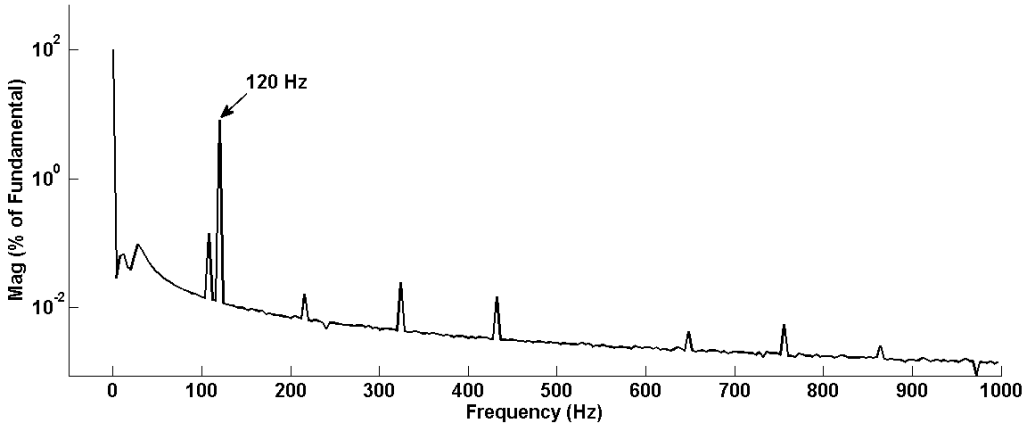

Fig. 33. DFIG with stator voltage unbalance using conventional control A) Stator power command and output B) FFT of reactive power

4.2 Experimental results

The modified control method is applied to a laboratory set up of a 7.5hp 4-pole 230v GE tri-clad doubly-fed machine. The DFIG is driven by a DC motor at a constant speed. The stator of the DFIG is connected to a balanced three phase resistive load. The rotor is fed through a 3 phase SEMIKRON IGBT-based inverter. A power supply is used to supply the DC voltage to the inverter. An optical encoder with a resolution of 2048 pulses per revolution is mounted on the shaft of the DFIG for position and speed measurements. Since the system is three-wire with no neutral connection, two of the rotor and stator phase currents are sensed using Hall Effect sensors. A block diagram of the experimental setup is shown in Fig. 34.

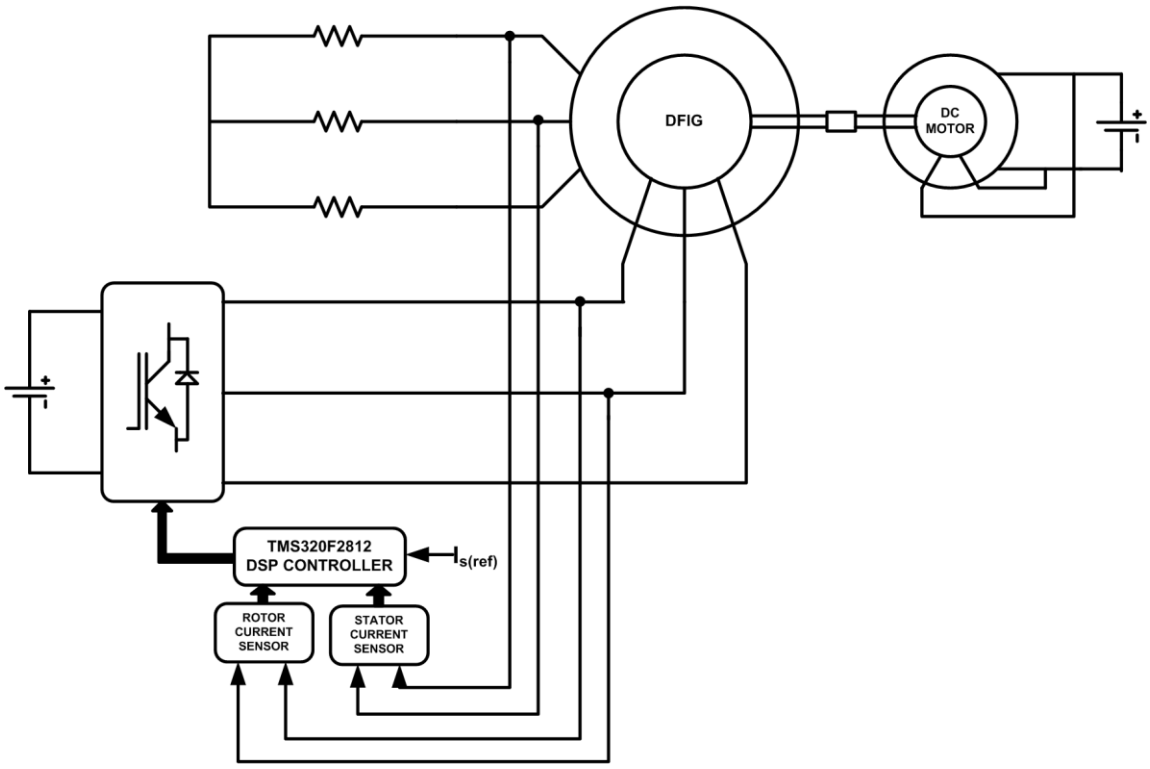

Fig. 34. Block diagram of experimental set-up

TMS320F2812 Texas Instruments DSP Controller is used to digitally implement the control algorithm. A signal conditioning circuit is used to interface the DSP with the current sensors and gate drive circuits of the inverter. Since the stator is connected to a resistive load the closed-loop is modified to control the current injected into the stator. For a fixed load resistance this fixes the power delivered to the stator and the voltage across the load resistors. The required stator frequency is given as an input to the DSP. The switching pattern is generated using Space Vector Pulse Width Modulation (SVPWM). The software for the DSP controller is written in C language and is built in a modular format. Texas Instruments C28x IQmath Library is used to handle the floating point arithmetic operations. The main modules and their functions are listed below.

- Ramp generator – generates the stator angle based on the required stator frequency
- Current measurement – uses 4 ADC channels to measure the currents through the current sensing circuits
- Clarke module – transforms variables from stationary 3 axis to stationary 2 axis reference frame
- Park's Module – transforms variables from stationary 2 axis to arbitrary rotating 2 axis reference frame
- Flux Estimator – calculates the stator flux from the stator currents and the resistance of the balanced three phase load using trapezoidal approximation for integration. The flux is used to calculate the command rotor currents using (2.40) and (2.41) for the current loop. To eliminate the errors cause due to pure

integration compensating terms are added through a PI controller. The stator flux is also estimated using the machine inductances from (2.30) and the error is fed to the PI controller.

- Speed Measurement – Uses the Quadrature Encoder Pulse (QEP) circuit in the DSP to determine the rotor position and calculate the rotor speed
- PI controller – digitally implements proportional integral control for closing the rotor current loop
- Feed forward compensator - adds compensating voltage terms to decouple the d and q axis rotor voltages
- Space Vector Module – calculates the duty cycles of each of the three legs of the inverter for a given modulating voltage signal using SVPWM.
- PWM Module – generates PWM signals based on the switching frequency and the required dead band.

The laboratory set-up of the DFIG is shown in Fig. 35 and Fig. 36. The machine parameters are determined using blocked rotor and no-load tests.

A static air gap eccentricity causes a $2f$ frequency component in the synchronous frame currents. In the abc frame this is a negative sequence current vector which is reflected as an unbalance in the stator phase currents.

A dynamic eccentricity causes a $2f - 2f_r$ frequency component in the synchronous frame currents. In the abc frame this is reflected as a $2f_r - f$ component in the stator phase currents.

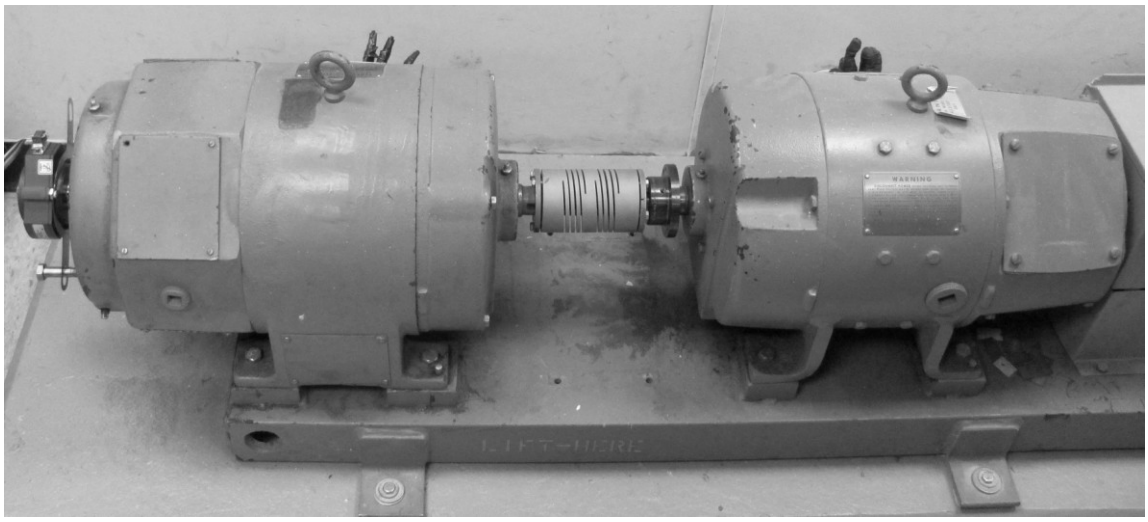

Fig. 35. Laboratory set-up of DFIG

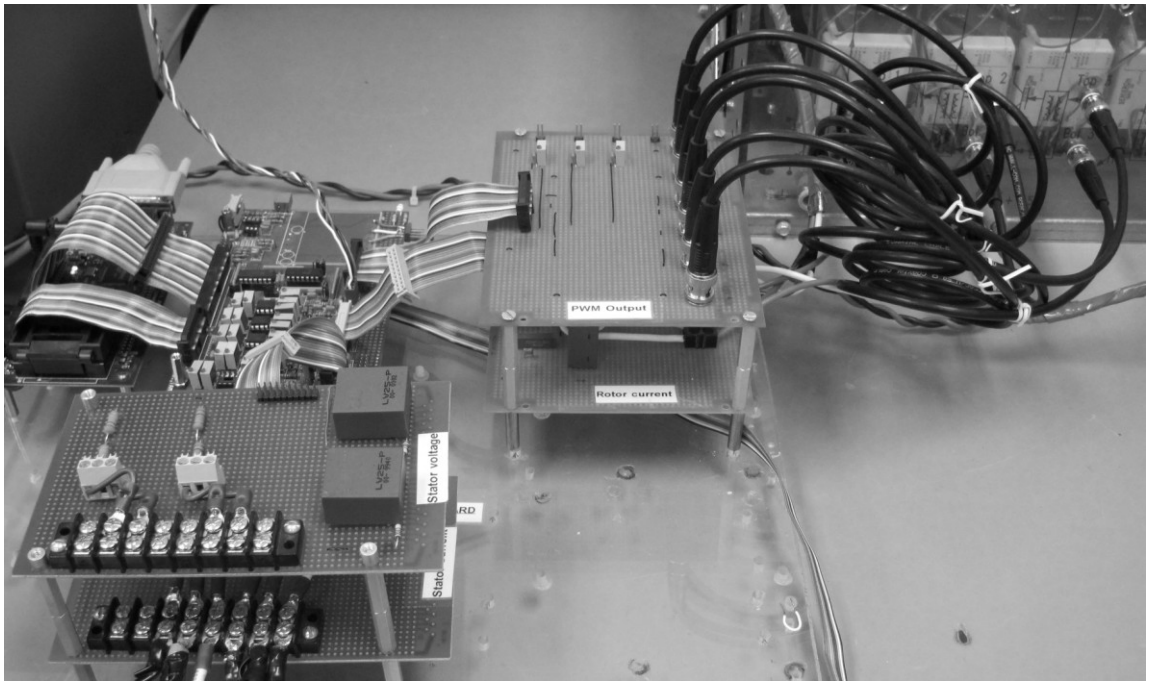

Fig. 36. DFIG control circuit

The amount of inherent eccentricity in the machine is determined by identifying these signatures in the phase currents. Since the signature frequency for dynamic eccentricities is dependent on the rotor speed, the stator current spectrum is obtained for four different rotor speeds using a spectrum analyzer. The stator frequency is fixed at 60 Hz which acts as the base frequency. The rotor electrical speed reference is increased from 0.65 to 0.8 in increments of 0.05. The FFT of A phase current in shown in Fig. 37 - Fig. 40.The current reference is fixed at 0.02p.u (0.832 A). The base current is 42A.

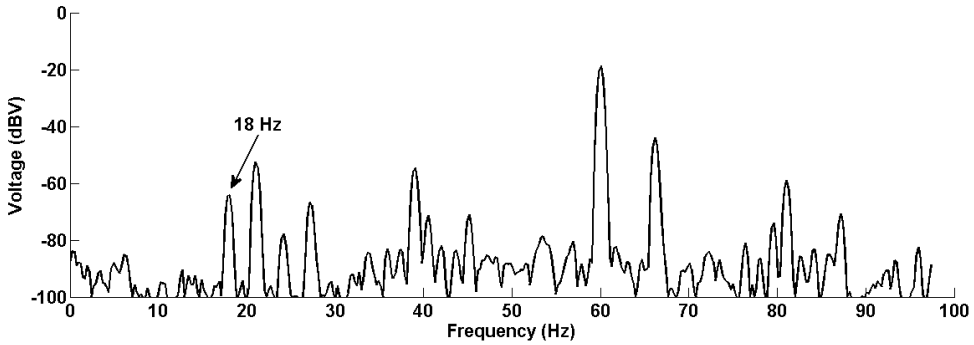

Fig. 37. Stator phase current spectrum at rotor electrical speed of 0.65p.u (1170 rpm).

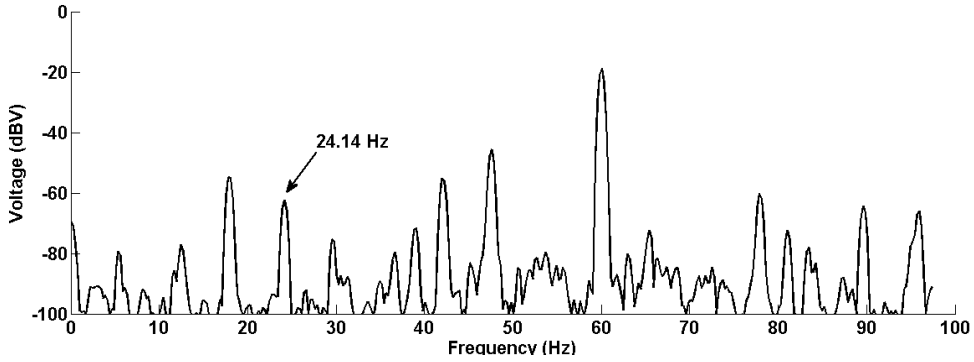

Fig. 38. Stator phase current spectrum for rotor electrical speed of 0.701p.u (1262 rpm).

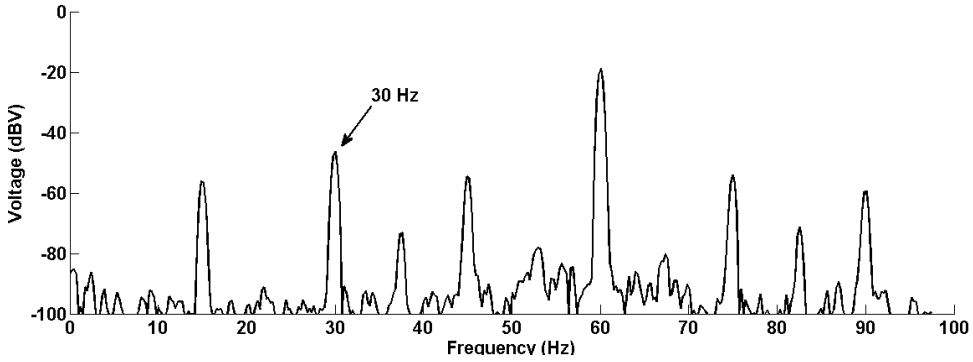

Fig. 39. Stator phase current spectrum for rotor electrical speed of 0.75p.u (1350 rpm).

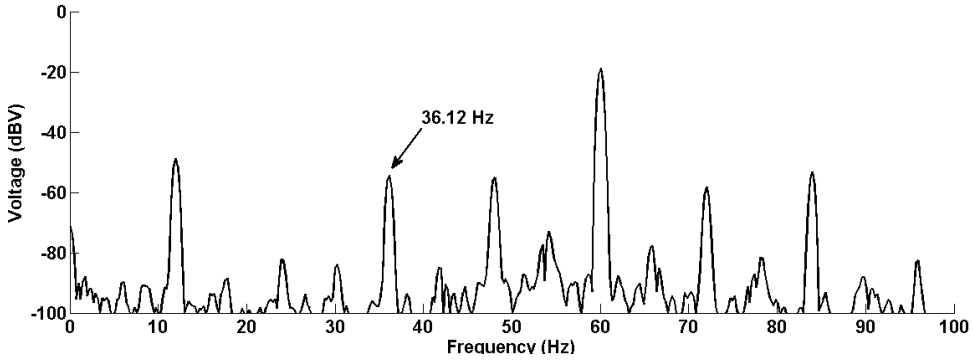

Fig. 40. Stator phase current spectrum for rotor electrical speed of 0.801p.u (1442 rpm).

The above waveforms indicate that the DFIG has an inherent dynamic eccentricity in the air gap. To identify static eccentricities the RMS phase currents are measured. Fig. 41 shows that there is an unbalance in the stator phase currents. This can be caused by static eccentricity or electrical unbalances in the stator windings or load resistance. To test the operation of the controller the stator current command is changed from 0.01p.u to 0.03p.u. The change in the stator phase current is shown in Fig. 42.

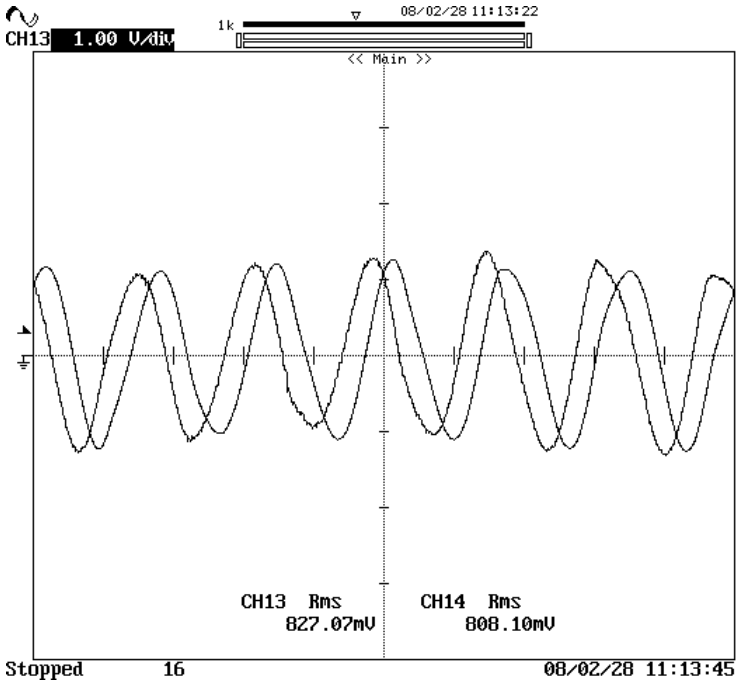

Fig. 41. Instantaneous current waveforms of A (channel 13) and B (channel 15) phase

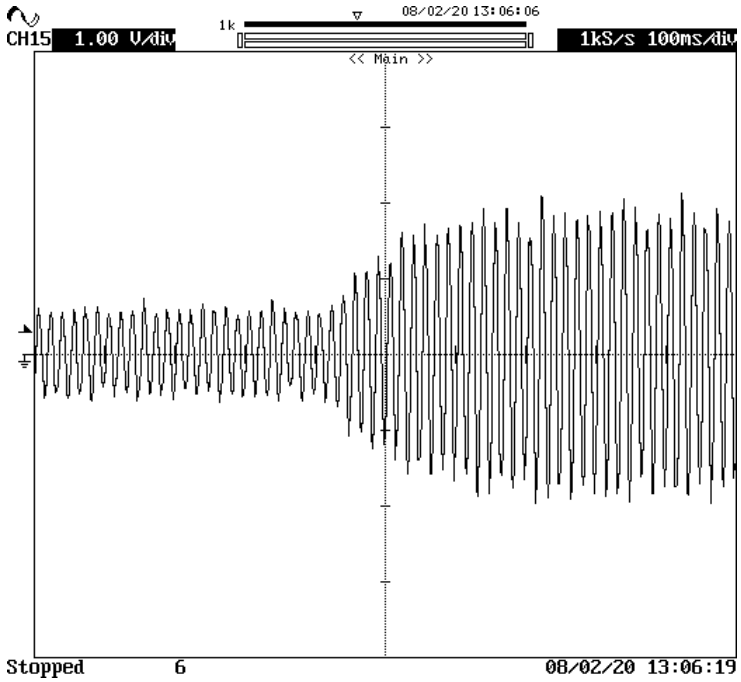

Fig. 42. Change in current command from 0.01p.u (0.41A) to 0.03p.u (1.24A)

5. CONCLUSIONS

This thesis provides a diagnostic control algorithm to detect and isolate air gap eccentricities in DFIGs operated in closed-loop. A model of the DFIG with static and dynamic eccentricity in air gap is built using Modified Winding Function Theory (MWFT). The effect of closed-loop control on the fault signatures is studied and a modification in the control scheme is proposed to enable detection and isolation of eccentricity faults from other faults like electrical unbalances and load torque oscillations that produce similar signatures. The effectiveness of the proposed modifications is verified using simulation and preliminary experiments on a laboratory set-up. The presented control method can also be used to predict the amount of eccentricity based on the extent of deviation of stator reactive power from the command. This work can be further extended by incorporating the saturation effects of L_m in the controller to improve the accuracy of the diagnosis.

REFERENCES

[1] Wind Energy Program (U.S.) and National Renewable Energy Laboratory (U.S.), "Wind power today: Wind Energy Program highlights." Washington, DC: Produced for the U.S. Dept. of Energy by the National Renewable Energy Laboratory, 1997, p. v.

[2] R. W. Thresher, M. Robinson, and P.Veers."The future of wind energy technology in the United States." Presented at the 2008 World Renewable Energy Congress, Glasgow, Scotland, July 19-25, 2008. Available: http://purl.access.gpo.gov/GPO/LPS108344

[3] I. Munteanu, A. I. Bratku, N.-A. Cutululis, and E. Ceanga, *Optimal Control of Wind Energy Systems Towards a Global Approach*. London: Springer, 2008.

[4] E. Spooner and A. C. Williamson, "Direct coupled, permanent magnet generators for wind turbine applications," *IEEE Proc. Electr. Power Appl.,* vol. 143, pp. 1-8, Jan 1996.

[5] S. Nandi, H. A. Toliyat, and X. D. Li , "Condition monitoring and fault diagnosis of electrical motors - A review," *IEEE Trans. Energy Convers.,* vol. 20, pp. 719-729, Dec 2005.

[6] B. Li, M.-Y. Chow, Y. Tipsuwan, and J. C. Hung, "Neural-network-based motor rolling bearing fault diagnosis," *IEEE Trans. Ind. Electron.,* vol. 47, pp. 1060-1069, Oct 2000.

[7] J. Penman, H. G. Sedding, B. A. Lloyd, and W. T. Fink, "Detection and location of interturn short circuits in the stator windings of operating motors," *IEEE Trans. Energy Convers.,* vol. 9, pp. 652-658, Dec 1994.

[8] X. H. Huang, T. G. Habetler, and R. G. Harley, "Detection of rotor eccentricity faults in a closed-loop drive-connected induction motor using an artificial neural network," *IEEE Trans. Power Electron.,* vol. 22, pp. 1552-1559, Jul 2007.

[9] A. Bellini, F. Filippetti, G. Franceschini, and C. Tassoni, "Closed-loop control impact on the diagnosis of induction motors faults," *IEEE Trans. Ind. Appl.,* vol. 36, pp. 1318-1329, Sep-Oct 2000.

[10] A. Stefani, A. Yazidi, C. Rossi, F. Filippetti, D. Casadei, and G.-A. Capolino, "Doubly fed induction machines diagnosis based on signature analysis of rotor modulating signals," *IEEE Trans. Ind. Appl.,* vol. 44, pp. 1711-1721, Nov-Dec 2008.

[11] R. R. Schoen and T. G. Habetler, "Effects of time-varying loads on rotor fault-detection in induction machines," *IEEE Trans. Ind. Appl.,* vol. 31, pp. 900-906, Jul-Aug 1995.

[12] L. Wu, B. Lu, T. G. Habetler, and R. G. Harley , "Improved online condition monitoring using static eccentricity-induced negative sequence current information in induction machines," *Proc. IECON'05,* 2005, pp. 1737-1742.

[13] M. Drif and A. J. M. Cardoso, "Airgap-eccentricity fault diagnosis, in three-phase induction motors, by the complex apparent power signature analysis," *IEEE Trans. Ind. Electron.,* vol. 55, pp. 1404-1410, Mar 2008.

[14] T. M. Wolbank and P. E. Macheiner, "Monitoring of static and dynamic air gap eccentricity of inverter fed induction machine drives," *Proc. IECON'06,* 2006, pp. 4040-4045.

[15] N. A. Al-Nuaim and H. A. Toliyat, "A novel method for modeling dynamic air gap eccentricity in synchronous machines based on modified winding function theory," *IEEE Trans. Energy Convers.,* vol. 13, pp. 156-162, Jun 1998.

[16] R. Datta and V. T. Ranganathan, "Variable-speed wind power generation using doubly fed wound rotor induction machine - A comparison with alternative schemes," *IEEE Trans. Energy Convers.,* vol. 17, pp. 414-421, Sep 2002.

[17] C.-M. Ong, *Dynamic Simulation of Electric Machinery: Using MATLAB/SIMULINK*. Upper Saddle River, NJ: Prentice Hall PTR, 1998.

[18] D. W. Novotny and T. A. Lipo, *Vector Control and Dynamics of AC Drives*. Oxford, New York: Oxford University Press, 1996.

[19] I. Boldea, *The Electric Generators Handbook. Variable Speed Generators*. Boca Raton, FL: CRC/Taylor & Francis, 2006.

[20] G. Tapia, A. Tapia, and J. X. Ostolaza, "Two alternative modeling approaches for the evaluation of wind farm active and reactive power performances," *IEEE Trans. Energy Convers.,* vol. 21, pp. 909-920, Dec 2006.

[21] J. P. A. Vieira, M. V. A. Nunes, U. H. Bezerra, and A. C. do Nascimento, "Designing optimal controllers for doubly fed induction generators using a genetic algorithm," *IET Generation Transmission & Distribution,* vol. 3, pp. 472-484, May 2009.

[22] L. Frosini and P. Pennacchi, "Detection and modelling of rotor eccentricity in electrical machines - an overview," *Vibrations in Rotating Machinery,* vol. 2004, pp. 501-510, 2004.

VITA

Vivek Meenakshi Sundaram received his Bachelor of Technology degree in Electrical and Electronics Engineering in 2008 from the National Institute of Technology, Trichy, India. He worked in the Advanced Electric Machines and Power Electronics Laboratory in the Department of Electrical Engineering at Texas A&M University under the guidance of Dr. Hamid Toliyat and obtained his Master of Science in Electrical Engineering in May 2011. He is currently working toward a PhD degree in Electrical Engineering under the guidance of Dr.Toliyat.

He may be reached at vivek5186@gmail.com or through the Department of Electrical and Computer Engineering, Texas A&M University, 3128 TAMU, College Station, Texas 77843.